Computer Methods in Applied Mechanics and Engineering 436 (2025) 117696

Contents lists available at ScienceDirect

Comput. Methods Appl. Mech. Engrg.

journal homepage: www.elsevier.com/locate/cma

A phase field formulation for modelling fracture of nearly incompressible hyperelastic materials

Deepak George [a], Shabnam Konica [b], Ian Masters [a], Mokarram Hossain [a,*]

[a] Zienkiewicz Institute for Modelling, Data and AI, Faculty of Science and Engineering, Swansea University, SA1 8EN, Swansea, United Kingdom
[b] School of Engineering, Brown University Providence, RI, USA

ARTICLE INFO

Keywords:
Phase field modelling
Mixed formulation
Finite strain fracture
Hyperelastic material
Incompressibility

ABSTRACT

Flexible materials are integral to modern applications due to their unique properties, particularly their ability to stretch and resilience to fracture. However, predicting the fracture behaviour of these materials through simulations remains challenging, primarily due to the lack of numerical robustness. This study proposes a rate-independent phase field model to predict finite strain fracture in nearly incompressible hyperelastic materials. A Griffith-type criterion is used to predict the fracture behaviour, with a relaxation of the incompressibility constraint in damaged elements, thus allowing crack propagation without affecting the intact material. A novel mixed formulation is developed using a quadratic dissipation function originally proposed by Ambrosio and Tortorelli (AT2) for the phase field method, incorporating two history fields to prevent crack healing. Spatial discretisation is achieved using linear approximations for the displacement and damage fields, whereas the pressure field is treated as discontinuous across the element boundaries (Q1Q0Q1 elements). The numerical algorithm is implemented within a finite element framework using a user-defined element (UEL) subroutine in ABAQUS, with a monolithic solver based on the Broyden–Fletcher–Goldfarb–Shanno (BFGS) technique to solve the global problem. Numerical trials confirmed that this is a robust algorithm that avoids excessive distortion of damaged elements, eliminating the need for adaptive meshing and distorted mesh deletion techniques. The algorithm is tested using three examples and is compared with experimental data. Reproduction of load–displacement behaviour and crack paths confirm the effectiveness of the method. The results indicate that the approach effectively predicts the fracture behaviour of nearly incompressible materials under large stretch conditions while maintaining numerical robustness. Additionally, the method successfully predicts multiple crack initiations, propagation paths, and their merging, consistent with various experimental observations. Consequently, this robust numerical scheme, involving 3D finite elements, can be readily applied to simulate various devices made of rubber-like materials, facilitating faster optimal design development and offers a promising alternative to multiple experiments and prototype testings resulting in a significant cost reduction.

1. Introduction

Products made of both artificial and natural rubbers have found a profound place in the modern society. They are widely used in many applications, including but not limited to, infrastructure, industrial, medical, transportation and lately electronic sectors.

* Corresponding author.
E-mail addresses: 1916377@swansea.ac.uk (D. George), shabnam_konica@brown.edu (S. Konica), i.masters@swansea.ac.uk (I. Masters), mokarram.hossain@swansea.ac.uk (M. Hossain).

https://doi.org/10.1016/j.cma.2024.117696
Received 3 September 2024; Received in revised form 2 December 2024; Accepted 20 December 2024
Available online 3 January 2025

Further, the advancements in additive manufacturing (3D printing) [1,2] technology have contributed to the widespread acceptance of such materials for everyday life. Elastomeric bearings [3] are widely used in bridge construction and seismic isolation applications while gaskets, seals and belts [4] are some of the classical applications of rubber-like materials in industry. Tyres and bushes [5] are common in transportation sectors. However, more recently scientists have also been looking at the applications of such materials where inflatable devices are used to power some of the pumping mechanisms used for medical applications [6]. One other application that is recently booming is the renewable energy generation using membrane materials which act as the primary mover [7,8]. They are also used for direct generation applications where an elastomeric material is used to constrain the electrodes of capacitors which generate a voltage difference upon the change in spacing during actuation [7].

Thanks to the widespread applications of such materials, computational modelling becomes a useful and efficient tool to design devices especially during their operation in finite strain regime that can mitigate the complexities arising from multiaxial testings [9]. However, the present computational tools are good at predicting the response of the structure in the elastic loading range and fails to capture its behaviour at limit state. Therefore, it is important to develop a robust computational tool that can predict the behaviour of the material at ultimate state. However, fracture phenomenon certainly introduces discontinuities in the solution which requires special treatment for solving using continuum damage models [10–12]. One of the most popular approaches is to approximate the sharp crack with a diffusive field thereby reinstating the continuity of the solution. However, such methods are still the topic of interests due to the requirement of numerical robustness and should be able to predict the behaviour of complex geometries with multiple crack nucleations, crack merging and branching making it difficult to solve in finite strain problems due to severe mesh distortion in damaged elements. Moreover, most hyperelastic materials exhibits very little volumetric strains compared to shear strains and are regarded as nearly incompressible if not perfectly incompressible. This results in severe volumetric locking if standard displacement-based finite element formulation is involved. To overcome this difficulty, the incompressibility constraint is enforced weakly resulting in an approximated quasi-incompressibility. Some of the popular methods of the quasi-incompressibility are $\mathbf{F}$-bar method by de Souza Neto et al. [13,14], reduced integration method with hourglass control [15,16], enhanced assumed strain energy method [17,18], mixed displacement–pressure two field formulation [19], three field displacement–pressure–Jacobian formulation [20]. Readers are directed to some of the works of Kadappa et al. [21–23] to understand the merits and applications of some these schemes.

One of the earlier attempts to model material degradation was by Kachanov et al. [24] where the effect of damage was considered as a reduction in the effective load bearing area of the material to model creep failure. However, such methods lead to the loss of ellipticity of the underlying differential equations. This is also evident from the mesh dependency of the finite element implementation which results in a vanishing damage zone while mesh refinement. Extended finite element method (XFEM) [25] is another approach which enriches the underlying solution functional by adding a discontinuous function which tracks the jumps in the displacement field during crack propagation. This method results in the decoupling of the crack path from the spacial discretisation, alleviating the need for remeshing. Nevertheless, this method requires the continuous monitoring of crack path and can become increasingly difficult in the case of 3D problems involving multiple cracks. However, XFEM can produce superior results compared to phase field modelling if quantities such as crack-tip stress and crack width are required [26]. Later non-local damage models were developed to overcome some of the difficulties of the local models. Here a local history variable which is usually a strain measure is used to drive a nonlocal damage variable thereby introducing an internal lengthscale. These are generally of two types; integral [27,28] and gradient types [8,29–31]. The gradient models, the damage regularisation occurs by adding gradients to the boundary value problem while the phase field models assumes a small fracture zone having sharp gradients. Peridynamics is another nonlocal approach in which the interaction between a material point and all other material points within a zone is captured [32]. Additionally, the method uses integral formulation whereby the calculation of the gradient over a discontinuity is not required as in other methods [33]. Material point method is a particle-based approach proposed by Sulsky et al. [34] which employs Lagrangian type particles with material properties and internal state variables whereas a background mesh is used to calculate the spatial gradient and divergence in a Eulerian sense. Recently, Liang et al. [35] proposed an extended material point method (XMPM) which enriches the displacement approximations in material point method similar to that of XFEM. Further, Zhang et al. [36] incorporated the phase field model with a material point method to model the fracture of rubber like materials. Configurational mechanics is another continuum mechanics framework which is particularly effective in modelling heterogeneous materials [37–39]. The method has been successfully used to model fracture problems, where the configurational force at the crack-tip is same as the $J-$ integral. Recently, Moreno-Mateos and Steinmann [40,41] illustrated the effectiveness of this method to capture the crack-tip blunting effect from the electro-mechanical actuation.

In the context of finite strain, Miehe and Schänzel [42] presented a rate-independent phase field model for fracture of rubbery materials. They used a compressible neo-Hookean material description to model the behaviour of the material. Hesch and Weinberg [43] proposed a multiplicative split of the principal stretches to identify its tension components which in turn drives the crack. Later, Borden et al. [44] illustrated the effects of stress triaxiality in crack nucleation for ductile fracture using finite strain theory. Further, Tang et al. [45] demonstrated the effectiveness of a compressible neo-Hookean model with a principal stretch-based energy split over a deviatoric–volumetric split to identify the tension part responsible for the crack propagation. They also reported that the deviatoric–volumetric split based model leads to an earlier termination of computation resulting in the partial development of phase field. The rate-dependent effects of rubber was first incorporated by Loew et al. [46] which accounted for viscosity in both the strain energy density function and the crack driving force. This was further modified for general viscoelastic polymers by Yin and Kaliske [47] to account for only the elastic stored energy for crack driving force. A fourth order phase field model for hyperelasticity was proposed by Fan et al. [48]. Further, numerous researchers have looked at incorporating phase field modelling into finite strain theory for various applications namely; general hyperelastic and viscoelastic materials [49–56], composites [57–63], biological

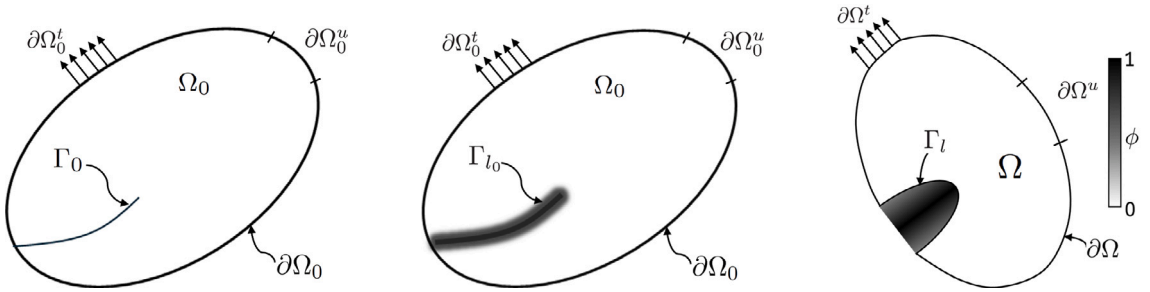

(a) Sharp crack in the reference configuration

(b) Sharp crack approximation in the reference configuration.

(c) Crack representation in the current configuration.

Fig. 1. Schematic representation of the sharp crack approximated by phase field ϕ over a smeared area in the reference and the current configurations.

tissues [64,65], dynamics [36,66–68], hydrogels [69–72], smart materials [41,73], plasticity [74], battery electrodes [75–77] etc. illustrating the versatility of phase field models.

Despite growing interests in modelling fracture of polymeric materials, only a very few researchers have looked at incorporating the incompressibility constraint. Some researchers have used plane stress elements whereby the incompressibility is accounted for while calculating the out of plane stretch of the elements [46,78–83]. However, such models are only limited to a few applications where a plane stress assumption holds. Thus, it is important to develop 3D elements which can effectively account for the incompressibility in the material. To account for this, Ma et al. [84] proposed a mixed displacement–pressure formulation. Similarly, Li and Bouklas [85] used a mixed formulation based on a micromechanically motivated constitutive model, and proposed the need to degrade the bulk modulus faster than the shear modulus to realise crack opening. Within the finite element framework, the displacement degrees of freedom were approximated using quadratic shape functions whereas linear approximations were used for both pressure and phase field degrees of freedom. Further, Li et al. [86] proposed a three field formulation based on enhanced assumed strain to solve the phase field problem for nearly incompressible hyperelastic materials. Later, Tian et al. [87] proposed a three field mixed pressure–displacement–damage formulation based on compressible neo-Hookean material model. They used linear interpolations for displacement and damage fields along with a discontinuous approximation for the pressure field. Further, the study also establishes the requirement to degrade the bulk energy contribution faster than the shear energy contribution. An active set method was used to ensure damage irreversibility due to the use of the linear dissipation function (AT1) for the phase field scheme. The difficulties arising from distorted elements in the damage zone is alleviated by using an adaptive mesh deletion strategy. Despite demonstrating an effective algorithm, the use of deviatoric–volumetric split was detested in their work due to the lack of robustness. Shortly, Ang et al. [88] proposed a stabilised scheme for the coupled phase field model whereby a linear approximation is used for all the field variables. The perturbed Lagrangian scheme along with a compressible neo-Hookean model was used to realise the incompressibility of the hyperelastic material.

To the best of the author's knowledge there has been no attempt to use an incompressible hyperelastic model based on the classical deviatoric–volumetric split approach to predict the fracture behaviour of rubber-like materials that can resolve complex fracture problems without using an adaptive meshing/mesh deletion technique. Hence, to understand the fracture behaviour of rubber-like materials, we propose a phase field fracture model coupled with a nearly incompressible hyperelastic material model. The numerical inconsistencies arising from the incompressibility of the material are overcome by employing a perturbed Lagrangian scheme resulting a coupled three field formulation similar to that of Li and Bouklas [85]. Despite the popularity of the well established staggered scheme, we propose for the first time, to employ a monolithic solver with a Broyden–Fletcher–Goldfarb–Shanno (BFGS) technique along with an adaptive stepping scheme to solve the coupled global problem. The effectiveness of the scheme is illustrated using multiple examples where the numerical predictions are compared with experimental results involving both simple and complex fracture behaviour.

The article has been composed in the following manner. Section 1 gives a brief introduction to the topic along with a literature review and establishes the need for the present study. The phase field damage approach is presented in Section 2. The section starts by establishing the kinematics of the nonlinear problem. Further, a description of the phase field models is provided along with a discussion of the constitutive models and the total potential energy of the mixed formulation is established. Now Section 3 describes the variational formulation of the problem and derives the strong forms. The thermodynamic consistency and the damage irreversibly are established and illustrated with the help of a 1D problem. Lastly, the section also describes the spatial discretisation and establishes the linearised problem. The proposed numerical framework is tested in Section 4 with the help of three distinct examples. Finally the article is concluded by a brief summary of the findings in Section 5.

2. Phase field damage modelling

Let us consider a body $\Omega_0 \subset \mathbb{R}^n$ defined in the reference configuration bounded by $\partial\Omega_0 \subset \mathbb{R}^{n-1}$ having a discontinuity Γ_0 as shown in Fig. 1. Upon action of external forces, the body is transformed to its current configuration Ω such that the deformation

map from point $\mathbf{X} \in \Omega_0$ to $\mathbf{x} \in \Omega$ is denoted by $\boldsymbol{\varphi} : \Omega_0 \rightarrow \Omega$. Further, the discontinuity in the continuum arising from cracks denoted as an internal boundary Γ_0 is represented in a smeared fashion such that a damage related scalar quantity ϕ is introduced where ϕ varies from 0 (for a pristine state) to 1 (for a fully damaged state). Following are the definitions of some kinematic quantities used in this work. Firstly the displacement field is given by

$$\mathbf{u} = \boldsymbol{\varphi}(\mathbf{X}) - \mathbf{X} = \mathbf{x} - \mathbf{X} \tag{1}$$

Now the deformation gradient tensor $\mathbf{F}$ is defined by the spatial gradient of the deformation mapping

$$\mathbf{F} = \boldsymbol{\nabla}_0 \boldsymbol{\varphi} = \mathbf{I} + \boldsymbol{\nabla}_0 \mathbf{u} \tag{2}$$

Further, the Jacobian denoting the volume change is defined as $J = \det(\mathbf{F})$, and consequently, the deviatoric part of the deformation gradient is defined as $\bar{\mathbf{F}} = J^{-1/3}\mathbf{F}$. The right Cauchy–Green strain tensor and its deviatoric component is given by $\mathbf{C} = \mathbf{F}^T\mathbf{F}$ and $\bar{\mathbf{C}} = J^{-2/3}\mathbf{C}$, respectively. The first invariants of $\mathbf{C}$ and $\bar{\mathbf{C}}$ are represented, respectively, by I_1 and $\bar{I}_1$. Throughout the paper $\square_0$ and $\square$ represents the quantities at the reference and the spatial configurations, respectively.

2.1. Phase field formulation

The thermodynamic principle behind brittle fracture was first introduced by Griffiths [89] in 1921. An existing crack is assumed to propagate if the energy release rate of the crack exceeds certain critical value G_c known as the fracture toughness of a material. However, this theory lacks the prediction of crack nucleation. As such Francfort and Marigo [90] modified it based on the variational principle such that a crack nucleates and branches if the corresponding potential energy of the body is minimised:

$$\Pi_{\text{int}}(\mathbf{u}) = \int_{\Omega_0} \Psi_{\text{int}} \mathrm{d}V + \int_{\Gamma} G_c \mathrm{d}\Gamma \tag{3}$$

where, Γ is the crack surface. Further, the crack advances in the direction that leads to a minimum total potential energy. However, such a form leads to one of the main problems of fracture mechanics: that the displacement field $\mathbf{u}$ is discontinuous over the cracked surface Γ. Inspired by the work of Ambrosio and Tortorelli [91] in the field of image segmentation, Bourdin et al. [92] proposed a method in which an approximation of the Griffith's functional is considered in the neighbourhood volume of the crack such that $\mathbf{u}$ is continuous over the crack surface. This is achieved by introducing a damage order parameter ϕ which smears over the crack surface making it continuous,

$$\Pi_{\text{int}}(\mathbf{u}, \phi) = \int_{\Omega_0} g(\phi)\Psi_{\text{int}} \mathrm{d}V + \int_{\Omega_0} G_c \gamma(\phi, \boldsymbol{\nabla}_0 \phi) \mathrm{d}V \tag{4}$$

Here, $g(\phi)$ is the degradation function and γ is the crack surface density function dependent on ϕ and $\boldsymbol{\nabla}_0\phi$ such that the product $G_c\gamma$ represents the critical fracture energy per unit volume. This step essentially allowed the approximation of the surface integral of crack area to a volume integral as:

$$\int_{\Gamma_0} G_c \mathrm{d}A \approx \int_{\Omega_0} G_c \gamma(\phi, \boldsymbol{\nabla}_0 \phi) \mathrm{d}V \tag{5}$$

Following some of the pioneering works in the field [92–95], a standard definition for the crack density function γ reads as

$$\gamma(\phi, \boldsymbol{\nabla}_0 \phi) = \frac{1}{4c_w}\left[\frac{w(\phi)}{l} + l\boldsymbol{\nabla}_0\phi \cdot \boldsymbol{\nabla}_0 \phi\right] \tag{6}$$

where, $w(\phi)$ is the dissipation function, l is the length scale factor deciding the extend of regularisation and $c_w = \int_0^1 \sqrt{w(\delta)}\mathrm{d}\delta$. Further, $w(\phi)$ has to fulfil the following conditions [96,97]:

$$w(0) = 0, \quad w(1) = 1, \quad w'(\phi) \geq 1 \quad 0 \leq \phi \leq 1. \tag{7}$$

The present study uses the AT2 method proposed by Ambrosio and Tortorelli [92,98] where,

$$w(\phi) = \phi^2 \quad \text{and} \quad c_w = \frac{1}{2} \tag{8}$$

It may be noted that the discussions presented in this study holds well for other versions of the phase field model and is straightforward to implement by altering the $w(\phi)$ and c_w. A popular choice of $w(\phi) = \phi$ results in the so called AT1 model and is preferred by some researchers due to their initial elastic region and damage starts once the critical stress has reached. While, the method is well suited for rigid metal-like materials, its suitability for rubber-like material is questionable. Unlike metals, rubber-like materials can sustain large stretch values before failure. While the catastrophic failure happens due to the rupture of polymer chains, other damage mechanism like chain pull out and bond breakage can happen while the material is being stretched [42]. This effect is further exasperated in case of filled rubbers where the disruption of the bond between the rigid filler and the polymer material starts at low strain levels [99]. While the difference in accuracy of both the schemes for elastomeric materials are not studied extensively in the literature, the work of Kristensen et al. [100] shows promising results for infinitesimal strain problems. As a result, we emphasise on the AT2 model in the present study. Thus, the total potential energy of the system at finite strain reads as:

$$\Pi_{\mathbf{u}-\phi} = \int_{\Omega_0} g(\phi)\Psi_{\text{int}}(\mathbf{F})\mathrm{d}V + \int_{\Omega_0} \frac{G_c}{2}\left[\frac{\phi^2}{l} + l\boldsymbol{\nabla}_0\phi \cdot \boldsymbol{\nabla}_0\phi\right]\mathrm{d}V - \Pi_{\text{ext}} \tag{9}$$

where, Π_{ext} is the potential energy due to external contribution and reads as

$$\Pi_{\text{ext}} = \int_{\Omega_0} \bar{\mathbf{B}} \mathrm{d}V + \int_{\Gamma_{0N}} \bar{\mathbf{T}} \mathrm{d}A \tag{10}$$

where, $\bar{\mathbf{B}}$ is the body force contribution and $\bar{\mathbf{T}}$ is the traction force represented in the reference configuration.

2.2. Hyperelastic material model for nearly incompressible materials

In this work, we follow the deviatoric–volumetric split of the strain energy density function as

$$\Psi_{\text{int}}(\mathbf{C}) = g(\phi)\Psi_{\text{iso}}(\bar{\mathbf{C}}) + f(\phi)\Psi_{\text{vol}}(J) \tag{11}$$

Such a split decouples the isochoric and volumetric deformation of the material and is dependent on the invariants of $\bar{\mathbf{C}}$ and the volume change J. Some of the works of Steinmann et al. [101], Hossain and Steinmann [102], Kadappa and Hossain [21], Marckmann and Verron [103] shall be referred for a detailed understanding of such models. On selecting a simple neo-Hookean model for the nearly incompressibility, $\Psi_{\text{iso}}(\bar{\mathbf{C}}, J) = \frac{\mu}{2}\left[\bar{I}_1 - 3\right]$ and $\Psi_{\text{vol}}(J) = \frac{K}{2}[J-1]^2$ the first Piola–Kirchhoff stress are derived as [102,104,105]

$$\mathbf{P} = \frac{\partial \Psi_{\text{int}}}{\partial \mathbf{F}} = g(\phi)\mathbf{P}_{\text{iso}} + f(\phi)\mathbf{P}_{\text{vol}} = g(\phi)\mu J^{-2/3}\left[\mathbf{F} - \frac{I_1}{3}\mathbf{F}^{-T}\right] + f(\phi)Jp\mathbf{F}^{-T} \tag{12}$$

where, μ is the shear modulus, K is the bulk modulus and p is the hydrostatic pressure defined as $p = \frac{\partial \Psi_{\text{vol}}}{\partial J}$. One of the most common volumetric energy functions, $\Psi_{\text{vol}} = \frac{K}{2}[J-1]^2$ is used here and readers are directed to the work of Kadapa et al. [21] for a detailed comparison of the effects of other volumetric functions.

2.3. Quasi-incompressibility and mixed formulation

For the accurate simulation of the incompressible nature of rubber-like materials, we chose to follow the mixed displacement–pressure–damage formulation here. The perturbed Lagrangian scheme is adopted to modify the elastic strain energy density function discussed in the previous section. The modified total potential energy functional of the system can be expressed as

$$\Pi_{\mathbf{u}-p-\phi} = \int_{\Omega_0} g(\phi)\Psi_{\text{iso}}(\bar{\mathbf{C}})\mathrm{d}V + \int_{\Omega_0} \Psi_{PL}\mathrm{d}V + \frac{G_c}{2}\int_{\Omega_0}\left[\frac{\phi^2}{l} + l\boldsymbol{\nabla}\phi\cdot\boldsymbol{\nabla}\phi\right]\mathrm{d}V - \Pi_{\text{ext}} \tag{13}$$

Here, Ψ_{PL} imposes the incompressibility constraint that can be defined as

$$\Psi_{PL} = \frac{p}{K}\left[\frac{\partial \Psi_{\text{vol}}}{\partial J} - \frac{p}{2}\right] \tag{14}$$

However, within the framework of phase field damage modelling, the volumetric contribution is also degraded using a degradation function $f(\phi)$ similar to $g(\phi)$ and the modified Ψ_{PL} incorporating the definition of $\Psi_{\text{vol}} = f(\phi)\Psi_{\text{vol}}$ is expressed as [85]

$$\Psi_{PL} = \frac{p}{K}\left[f(\phi)\frac{\partial \Psi_{\text{vol}}}{\partial J} - \frac{p}{2}\right] = p\left[f(\phi)[J-1] - \frac{p}{2K}\right] \tag{15}$$

Here it is important to note that as the Poisson's ratio (ν) of the material approaches 0.5, the bulk modulus $K \to \infty$ and $\frac{p^2}{2K} = 0$. The method presented here closely follows the implementation of Li and Bouklas [85]. The perturbed Lagrangian method for incompressibility has been successfully implemented in several multi-field problems [106–110] giving us the motivation for the present study.

3. Variational formulation and finite element implementation

Following the stationarity principle, the boundary value problem is governed by the principle of minimum potential energy, $\min\Pi(\boldsymbol{\varphi}, p, \phi,)_{\boldsymbol{\varphi},p,\phi}$, such that

$$\delta\Pi = \mathrm{D}\Pi[\delta\boldsymbol{\varphi}] + \mathrm{D}\Pi[\delta p] + \mathrm{D}\Pi[\delta\phi] = 0 \tag{16}$$

i.e.,

$$\begin{aligned} &\delta_{\boldsymbol{\varphi}}\Pi(\boldsymbol{\varphi}, p, \phi) = 0 \quad \forall \quad \delta\boldsymbol{\varphi} \\ &\delta_{p}\Pi(\boldsymbol{\varphi}, p, \phi) = 0 \quad \forall \quad \delta p \\ &\delta_{\phi}\Pi(\boldsymbol{\varphi}, p, \phi) = 0 \quad \forall \quad \delta\phi \end{aligned} \tag{17}$$

leading to

$$\int_{\Omega_0} \mathbf{P} : \boldsymbol{\nabla}_0\delta\boldsymbol{\varphi} dV \; - \; \int_{\Omega_0} \bar{\mathbf{B}}\cdot\delta\boldsymbol{\varphi}\;\mathrm{dV} \; - \; \int_{\Gamma_{0n}} \bar{\mathbf{T}}\cdot\delta\boldsymbol{\varphi}\;\mathrm{dA} = 0 \tag{18}$$

$$\int_{\Omega_0}\left[f(\phi)[J-1] - \frac{p}{K}\right]\delta p\mathrm{d}V = 0 \tag{19}$$

$$\int_{\Omega_0}\left[f'(\phi)p[J-1] + g'(\phi)\Psi_{\text{iso}}(\bar{\mathbf{F}})\right]\delta\phi\mathrm{d}V + \frac{G_c}{l}\int_{\Omega_0}\left[\phi\delta\phi \; + \; l^2\nabla_0\phi\cdot\nabla_0\delta\phi\right]\mathrm{d}V = 0 \tag{20}$$

where, the components of the first Piola–Kirchhoff stress (PK1) can be identified as $\mathbf{P} = g(\phi)\frac{\partial \Psi_{\text{iso}}}{\partial \mathbf{F}} + f(\phi)pJ\mathbf{F}^{-T}$. The next step in the process is to establish the strong forms of the problem. The following relationships are applied into Eqs. (18) and (20),

$$\mathbf{P} : \boldsymbol{\nabla}_0 \delta\boldsymbol{\varphi} = \boldsymbol{\nabla}_0 \cdot [\delta\boldsymbol{\varphi} \cdot \mathbf{P}] - \delta\boldsymbol{\varphi} \cdot [\boldsymbol{\nabla}_0 \mathbf{P}] \tag{21}$$

$$\boldsymbol{\nabla}_0 \phi \cdot \boldsymbol{\nabla}_0 \delta\phi = \boldsymbol{\nabla}_0 \cdot [\delta\phi \boldsymbol{\nabla}_0 \phi] - \delta\phi \boldsymbol{\nabla}_0 \cdot [\boldsymbol{\nabla}_0 \phi] \tag{22}$$

and by using the Gauss's divergence theorem, the strong forms are obtained as

$$\boldsymbol{\nabla}_0 \cdot \mathbf{P} + \bar{\mathbf{B}} = \mathbf{0} \quad \text{in} \quad \Omega_0, \tag{23}$$

$$\mathbf{P} \cdot \mathbf{N} = \bar{\mathbf{T}} \quad \text{on} \quad \Gamma_{0N}, \tag{24}$$

$$f(\phi)[J-1] - \frac{p}{K} = 0 \quad \text{in} \quad \Omega_0 \tag{25}$$

$$\frac{G_c}{l}\left[\phi - l^2 \boldsymbol{\nabla}_0 \phi \cdot \boldsymbol{\nabla}_0 \phi\right] + g'(\phi)\mathcal{H}_1 + f'(\phi)p\mathcal{H}_2 = 0 \quad \text{in} \quad \Omega_0 \tag{26}$$

$$\boldsymbol{\nabla}_0 \phi \cdot \mathbf{N} = 0 \quad \text{on} \quad \Gamma_0 \tag{27}$$

The Eqs. (23) to (25) represent the linear momentum balance in the reference configuration and Eqs. (26) and (27) represent the balance equations associated with the phase field variable ϕ. It may be noted that a natural boundary condition such that $\boldsymbol{\nabla}_0 \phi \cdot \mathbf{N} = 0$ is considered for the phase field variable throughout the boundary of the domain. The damage driving force is purely energetic and is defined by $f := -\partial_\phi \Psi_{\text{int}} = -g'(\phi)\Psi_{\text{iso}} - f'(\phi)p[J-1]$, denoting that the evolution of crack is driven by the isochoric and the volumetric energy contribution. In order to prevent damage healing, $\mathcal{H}_1$ and $\mathcal{H}_2$ are introduced and are energy history variables [42,49] corresponding to the deviatoric and volumetric parts, respectively.

$$\begin{aligned} \mathcal{H}_1^{n+1} &= \begin{cases} \Psi_{\text{iso}} & \text{if} \quad \Psi_{\text{iso}} \geq \mathcal{H}_1^n \\ \mathcal{H}_1^n & \text{otherwise} \end{cases} \\ \mathcal{H}_2^{n+1} &= \begin{cases} [J-1] & \text{if} \quad [J-1] \geq \mathcal{H}_2^n \\ \mathcal{H}_2^n & \text{otherwise} \end{cases} \end{aligned} \tag{28}$$

where, $\square^{n+1}$ denotes the value of the variable corresponding to the current iteration. It is also important to note that the above choice of $\mathcal{H}_2$ prevents any damage evolution in compression zone detected by $J < 1$. In the context of a 1D problem, the governing equation for the damage variable in Eq. (26) reduces to the following quadratic equation in ϕ

$$\frac{G_c}{l}\phi + g'(\phi)\mathcal{H}_1 + f'(\phi)p\mathcal{H}_2 = 0 \tag{29}$$

$$-3p\mathcal{H}_2\phi^2 + \left[\frac{G_c}{l} + 2\mathcal{H}_1 + 6p\mathcal{H}_2\right]\phi - [2\mathcal{H}_1 + 3p\mathcal{H}_2] = 0 \tag{30}$$

whose solution can be found as

$$\phi = \frac{\frac{G_c}{l} + 2\mathcal{H}_1 + 6p\mathcal{H}_2 - \sqrt{\left[\frac{G_c}{l} + 2\mathcal{H}_1\right]^2 + 12\frac{G_c}{l}p\mathcal{H}_2}}{6p\mathcal{H}_2} \tag{31}$$

It may be noted that the other root of the quadratic equation is ignored as it results in $\phi > 1$. Following a similar procedure presented in [49], it can be shown that the constraints due to history field results in a damage field $\phi \in [0, 1]$. At small loadings,

$$\mathcal{H}_1 \approx \mathcal{H}_2 \approx \alpha \to 0 \qquad \Rightarrow \qquad \phi \approx \frac{\frac{G_c}{l} - \frac{G_c}{l}}{6p\mathcal{H}_2} \approx 0 \tag{32}$$

and for very large loadings, there exist three possible cases,

$$\mathcal{H}_1 \approx \mathcal{H}_2 \approx \alpha \to \infty \qquad \Rightarrow \qquad \phi \approx \frac{2 + 6p - \sqrt{4}}{6p} \approx 1 \tag{33}$$

$$\mathcal{H}_1 \ll \mathcal{H}_2 \approx \alpha \to \infty \qquad \Rightarrow \qquad \phi \approx \frac{\frac{G_c}{l\alpha} + 2\frac{\mathcal{H}_1}{\alpha} + 6p - \sqrt{\left[\frac{G_c}{l\alpha} + 2\frac{\mathcal{H}_1}{\alpha}\right]^2 + 12\frac{G_c}{l\alpha}p}}{6p} \approx 1 \tag{34}$$

$$\mathcal{H}_2 \ll \mathcal{H}_1 \approx \alpha \to \infty \qquad \Rightarrow \qquad \phi \approx \frac{\frac{G_c}{l} + 2\alpha + 6p\mathcal{H}_2 - \left[\frac{G_c}{l} + 2\alpha\right]}{6p\mathcal{H}_2} \approx 1 \tag{35}$$

3.1. Degradation function

The degradation function defines the transition of material from a virgin state to a fully cracked state and should be chosen such that

$$g(0) = 1, \quad g(1) = 0 \quad g'(\phi) \leq 0 \quad 0 \leq \phi \leq 1 \tag{36}$$

The choices of degradation functions used in the study are

$$g(\phi) = [1-\phi]^2 + \epsilon \tag{37}$$

$$f(\phi) = [1-\phi]^3 + \epsilon \tag{38}$$

and results in a faster degradation of the volumetric energy than the shear energy contribution enabling the gradual relaxation of the incompressibility constraint at the locations of damage accumulation. A similar approach has already been used by other researchers to overcome the difficulties in crack opening due to the incompressibility of the material [85,87,88]. Further, ϵ denotes the small value taken which accounts for the residual strength in the material after the fully damaged state. This also helps to keep the global stiffness matrix positive definite by preventing the diagonal terms from going to zero. However, in the present study, a sufficiently large *small residual* also prevents the excessive distortion of the damaged elements especially as it undergoes significant volume changes at advanced stages of fracture. Another effective approach in doing the same is as presented by Loew et al. [46] where they introduced an additional energy contribution Ψ_{res} along with the total energy density which has a value

$$\Psi_{\text{res}} = \epsilon_{\text{res}}[I_1 - 3] \tag{39}$$

in which ϵ_{res} is a sufficiently small value and Ψ_{res} is not degraded using the degradation function. The present study uses both the above approaches to solve different numerical examples.

3.2. Thermodynamic consistency and damage irreversibility

The stress-like thermodynamic forces that drive cracks can be derived for an isothermal, irreversible damage process by following the standard procedure. The rate of entropy production can be derived as

$$\dot{S} = \int_{\Omega_0} \left[\mathbf{P} : \dot{\mathbf{F}} - \dot{\Psi}\right] \mathrm{d}V \geq 0 \tag{40}$$

By using Eqs. (13), (40) can be rewritten as

$$\dot{S} = \int_{\Omega_0} \left[\mathbf{P} - \frac{\partial \Psi}{\partial \mathbf{F}}\right] : \dot{\mathbf{F}} \mathrm{d}V - \int_{\Omega_0} \left[f(\phi)[J-1] - \frac{p}{K}\right] \dot{p} \mathrm{d}V - \int_{\Omega_0} \left[\frac{G_c}{l}\phi + g'(\phi)\Psi_{\text{iso}}\right] \dot{\phi} \mathrm{d}V - \int_{\Omega_0} G_c l \boldsymbol{\nabla}_0 \phi \cdot \boldsymbol{\nabla}_0 \dot{\phi} \mathrm{d}V \geq 0 \tag{41}$$

Now by performing integration by parts and invoking the Gauss's divergence theorems, the strong forms in (23) to (27) are recovered.

The use of two degradation functions in the damage setting results in two different history variables relating to the deviatoric and volumetric responses. Hence it is important to ensure the irreversibility of the damage variable $\dot{\phi} \geq 0$.

Let us consider a simple uniaxial homogeneous deformation problem where the deformation gradient can be defined as

$$\mathbf{F} = \begin{bmatrix} \lambda & 0 & 0 \\ 0 & \lambda_T & 0 \\ 0 & 0 & \lambda_T \end{bmatrix} \tag{42}$$

where λ represents the stretch in the direction of the applied force and λ_T represents the stretches in the two lateral directions. Consequently, the volume change 'Jacobian' of the material can be expressed as

$$J = \det(\mathbf{F}) = \lambda \lambda_T^2 \tag{43}$$

Now the right Cauchy–Green tensor and the corresponding isochoric part can be expressed as

$$\mathbf{C} = \begin{bmatrix} \lambda^2 & 0 & 0 \\ 0 & \lambda_T^2 & 0 \\ 0 & 0 & \lambda_T^2 \end{bmatrix}, \quad \text{and } \bar{\mathbf{C}} = (\lambda\lambda_T^2)^{-\frac{2}{3}} \begin{bmatrix} \lambda^2 & 0 & 0 \\ 0 & \lambda_T^2 & 0 \\ 0 & 0 & \lambda_T^2 \end{bmatrix} \tag{44}$$

The corresponding first invariants are defined as

$$I_1 = \left[\lambda^2 + 2\lambda_T^2\right], \quad \text{and } \bar{I}_1 = (\lambda\lambda_T^2)^{-\frac{2}{3}}\left[\lambda^2 + 2\lambda_T^2\right] \tag{45}$$

Now the components of the damaged Cauchy stress can be expressed as

$$\sigma_{11} = g(\phi)\frac{2}{3}\mu[\lambda\lambda_T^2]^{-\frac{5}{3}}\left[\lambda^2 - \lambda_T^2\right] + f(\phi)p \tag{46}$$

$$\sigma_{22}, \sigma_{33} = g(\phi)\frac{1}{3}\mu[\lambda\lambda_T^2]^{-\frac{5}{3}}\left[\lambda_T^2 - \lambda^2\right] + f(\phi)p \tag{47}$$

where the pressure component p can be expressed as $p = K[J-1] = K[\lambda\lambda_T^2 - 1]$. Now the values of the lateral stretch λ_T can be found out by enforcing the stress-free boundary conditions such that $\sigma_{22} = \sigma_{33} = 0$. The resulting coupled nonlinear equation is solved using a Newton–Raphson technique to yield λ_T for the corresponding damage ϕ from Eq. (31). Fig. 2(a) illustrates the volume change vs. stretch for different values of the ratio $\gamma = \frac{K}{\mu}$. The effect of the incompressibility can be seen as a decrease in the change of volume with an increase in the bulk modulus. Further, the evolution of the damage for the 1D cyclic tension test where, the sample is stretched to six times its original length and unloaded completely, followed by stretching until failure is plotted in Fig. 2(b) which further demonstrates the effectiveness of the history variable in preventing damage healing. The damage value starts from zero for the unloaded case and increases to a value of 0.675 for a stretch of six. On unloading, ϕ remains constant throughout the unloading stage. An increase of damage is obtained as the reloading cycle reaches the stretch of six. On further loading, ϕ can be seen to approach one asymptotically. The mechanical response is illustrated by the stress–stretch diagram in Fig. 2(c). We observe

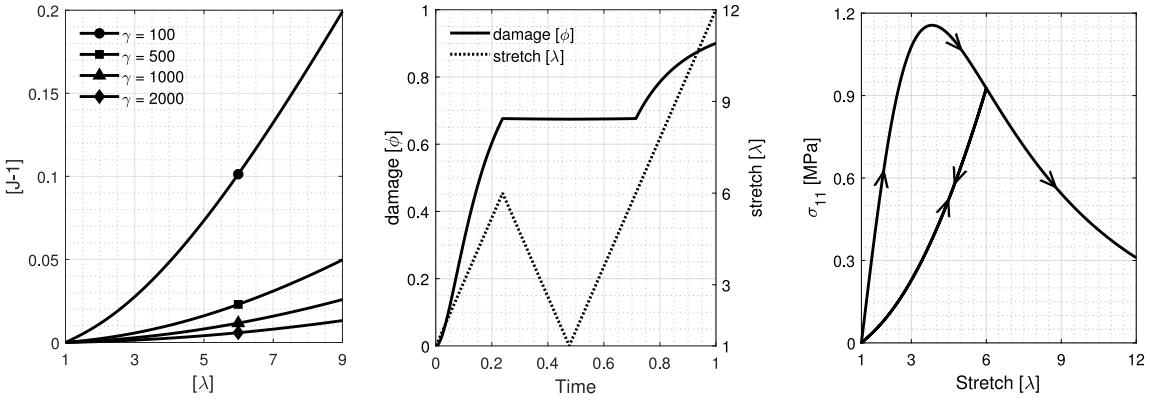

(a) Evolution of volume change. (b) Evolution of damage. (c) Evolution of stress.

Fig. 2. 1D Homogeneous deformation results. (a) shows the change in volume for different values of the ratio $\gamma = \frac{\kappa}{\mu}$. (b) represents the evolution of damage variable corresponding to a cyclic stretch as illustrated and (c) represents the Cauchy's stress subjected to damage as the sample undergoes the cyclic loading.

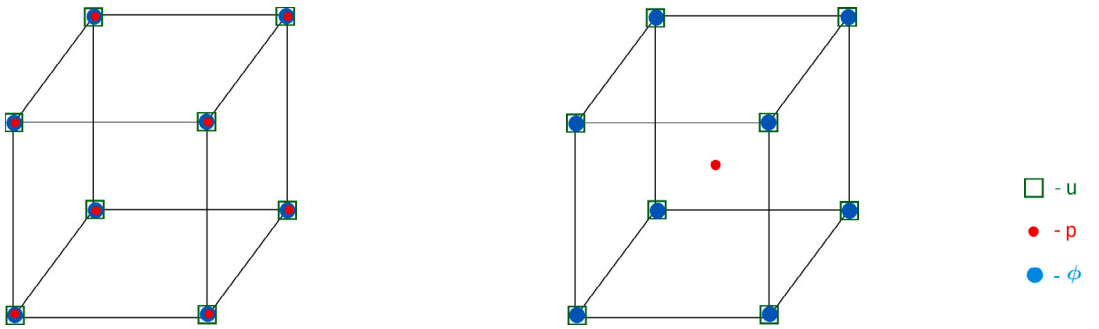

(a) Q1Q1Q1 (b) Q1Q0Q1

Fig. 3. Eight noded 3D brick elements adopted in the current study.

that the stress response of the sample softens as damage accumulates and reaches a peak value of around 1.14 MPa at a stretch of about four. On further loading, the stress drops until the unloading of the samples starts at a stretch of six. Subsequently, the sample is completely unloaded and reaches its original position. However, while unloading, the stress–stretch response follows a different path showing the effect of hysteresis represented by the area between the loading and unloading curves. On reloading the specimen, the stress–stretch response follows the unloading path until it reaches the loading path of the previous cycle and continues to degrade as $\phi \to 1$.

3.3. Viscous stabilisation and pseudo time dependency

In order to add a viscous regularisation term, we define the rate of potential energy functional $\dot{\Pi}$. This makes the formulation general and aids for the easy incorporation of viscoelasticity in future works. The rate functional is defined by

$$\dot{\Pi} = \int_{\Omega_0} \left[\mathbf{P} : \dot{\mathbf{F}} + \left[f(\phi)[J-1] - \frac{p}{K} \right] \dot{p} + \left[g'(\phi)\mathcal{H}_1 + f'(\phi)p\mathcal{H}_2 \right] \dot{\phi} \right] \mathrm{d}V + \int_{\Omega_0} G_c \left[\frac{\phi}{l}\dot{\phi} + l\boldsymbol{\nabla}_0\phi \cdot \boldsymbol{\nabla}_0\dot{\phi} \right] \mathrm{d}V + \int_{\Omega_0} \eta \frac{\dot{\phi}^2}{2} - \dot{\Pi}_{\text{ext}} \tag{48}$$

where, η is a viscous regularisation term that stabilises the energy dissipation especially when a brutal crack growth occurs. Further, the rate-independent energy functional is recovered as $\eta \to 0$. Now the variation of the above rate functional with respect to damage $\dot{\phi}$ yields the strong form:

$$\eta\dot{\phi} + \frac{G_c}{l}\left[\phi - l^2\boldsymbol{\nabla}_0\phi \cdot \boldsymbol{\nabla}_0\phi\right] + g'(\phi)\mathcal{H}_1 + f'(\phi)p\mathcal{H}_2 = 0 \quad \text{in} \quad \Omega_0 \tag{49}$$

Now the discretisation in terms of pseudo time t is given by [42]

$$\eta\frac{\phi - \phi_n}{\Delta t} + \frac{G_c}{l}\left[\phi - l^2\boldsymbol{\nabla}_0\phi \cdot \boldsymbol{\nabla}_0\phi\right] + g'(\phi)\mathcal{H}_1 + f'(\phi)p\mathcal{H}_2 = 0 \quad \text{in} \quad \Omega_0 \tag{50}$$

where, ϕ and ϕ_n represents the value of the damage field from the current and the previous time steps, respectively. The time step size is defined as $\Delta t := t_{n+1} - t_n > 0$.

3.4. Spatial discretisation

This section deals with the spacial discretisation of the domain and solution of the coupled nonlinear problem. The domain Ω_0 is discretised into n_{el} elements such that

$$\mathcal{B}_0 \approx \mathcal{B}_0^{\text{h}} = \bigcup_{\text{e}=1}^{n_{\text{el}}} \mathcal{B}_0^{\text{e}} \tag{51}$$

Here, each finite element $\mathcal{B}_0^{\text{e}}$ consists of $n^{\boldsymbol{\varphi}}$ nodes in space, n^p and n^ϕ nodes for pressure and phase field nodes, respectively. Further, the field variable $\boldsymbol{\varphi}$ and ϕ are approximated using the same shape functions as that of geometry $\mathbf{X}$ such that

$$\mathbf{X} \approx \mathbf{X}^{\text{h}} = \mathbf{N}_{\boldsymbol{\varphi}}\mathbf{X}^{\text{e}}, \qquad \boldsymbol{\varphi} \approx \boldsymbol{\varphi}^{\text{h}} = \mathbf{N}_{\boldsymbol{\varphi}}\boldsymbol{\varphi}^{\text{e}}, \qquad \phi \approx \phi^{\text{h}} = \mathbf{N}_{\phi}\phi^{\text{e}} \tag{52}$$

However, for the Q1Q0Q1 element adopted in the study (see Fig. 3(b)), $n_{\boldsymbol{\varphi}} = n_\phi \neq n_p$. Hence the approximation for the pressure is given by

$$p = \mathbf{N}_p\mathbf{p}^{\text{e}} = p_1 \quad \text{for} \quad n_p = 1 \tag{53}$$

Here $\mathbf{N}_{\boldsymbol{\varphi}}$ and $\mathbf{N}_\phi$ are the basis functions for the corresponding degrees of freedom given by

$$\mathbf{N}_{\boldsymbol{\varphi}} = \begin{bmatrix} N_\varphi^1 & 0 & 0 & \cdots & N_\varphi^{n^u} & 0 & 0 \\ 0 & N_\varphi^1 & 0 & \cdots & 0 & N_\varphi^{n^u} & 0 \\ 0 & 0 & N_\varphi^1 & \cdots & 0 & 0 & N_\varphi^{n^u} \end{bmatrix} \tag{54}$$

$$\mathbf{N}_\phi = \begin{bmatrix} N_\phi^1 & N_\phi^2 & N_\phi^3 & \cdots & N_\phi^{n^\phi} \end{bmatrix} \tag{55}$$

where, n^u and n^ϕ are the number of nodes corresponding to each degrees of freedom. Let the displacement vector in 3D space is given by $\boldsymbol{\varphi} = [u, v, w]^T$. The gradient of $\boldsymbol{\varphi}$ can be expressed in vector notation as

$$\boldsymbol{\nabla}\boldsymbol{\varphi} = \begin{bmatrix} \frac{\partial u}{\partial x} & \frac{\partial v}{\partial x} & \frac{\partial w}{\partial x} & \frac{\partial u}{\partial y} & \frac{\partial v}{\partial y} & \frac{\partial w}{\partial y} & \frac{\partial u}{\partial z} & \frac{\partial v}{\partial z} & \frac{\partial w}{\partial z} \end{bmatrix}^T \tag{56}$$

$$= \mathbf{G}_{\boldsymbol{\varphi}}\boldsymbol{\varphi}^e \tag{57}$$

On the substituting the approximations of displacement given in Eq. (52), the gradient operator is denoted in matrix notation as

$$\mathbf{G}_{\boldsymbol{\varphi}} = \begin{bmatrix} \frac{\partial N}{\partial x} & 0 & 0 & \frac{\partial N}{\partial y} & 0 & 0 & \frac{\partial N}{\partial z} & 0 & 0 \\ 0 & \frac{\partial N}{\partial x} & 0 & 0 & \frac{\partial N}{\partial y} & 0 & 0 & \frac{\partial N}{\partial z} & 0 \\ 0 & 0 & \frac{\partial N}{\partial x} & 0 & 0 & \frac{\partial N}{\partial y} & 0 & 0 & \frac{\partial N}{\partial z} \end{bmatrix}^T \tag{58}$$

Similarly, a divergence operator is defined as $\boldsymbol{\nabla}\cdot\boldsymbol{\varphi} = \mathbf{D}_{\boldsymbol{\varphi}}\boldsymbol{\varphi}$ where,

$$\mathbf{D}_{\boldsymbol{\varphi}} = \begin{bmatrix} \frac{\partial N}{\partial x} & \frac{\partial N}{\partial y} & \frac{\partial N}{\partial z} \end{bmatrix} \tag{59}$$

Now the Cauchy stress tensor is represented in a vector notation as

$$\boldsymbol{\sigma} = \begin{bmatrix} \sigma_{11} & \sigma_{21} & \sigma_{31} & \sigma_{12} & \sigma_{22} & \sigma_{13} & \sigma_{13} & \sigma_{23} & \sigma_{33} \end{bmatrix}^T \tag{60}$$

This results in the following weak forms in an elemental level.

$$\mathbf{R}_{\boldsymbol{\varphi}}^e = \int_\Omega \mathbf{G}_{\boldsymbol{\varphi}}^T\boldsymbol{\tau}\,\mathrm{d}V - \int_\Omega \mathbf{N}_{\boldsymbol{\varphi}}{}^T\mathbf{b}\,\mathrm{d}v - \int_{\Gamma_n} \mathbf{N}_{\boldsymbol{\varphi}}{}^T\mathbf{t}\,\mathrm{d}a \tag{61}$$

$$\mathbf{R}_p^e = \int_{\Omega_0} \mathbf{N}_p^T\left[f(\phi)[J-1] - \frac{p}{K}\right]\mathrm{d}V \tag{62}$$

$$\mathbf{R}_\phi^e = \int_{\Omega_0} \left[-G_c l\mathbf{B}_\phi^T\boldsymbol{B}_\phi\phi^{\text{e}} - \frac{G_c}{l}\mathbf{N}_\phi^T\phi - 2\mathbf{N}_\phi^T[1-\phi]\mathcal{H}_1 - 3\mathbf{N}_\phi^T[1-\phi]^2 p\mathcal{H}_2 + \eta\mathbf{N}_\phi^T\frac{\phi-\phi_n}{\Delta t}\right]\mathrm{d}V \tag{63}$$

where, $\boldsymbol{\tau} = J\boldsymbol{\sigma}$ is the Kirchhoff stress.

3.5. Linearisation and BFGS algorithm

The nonlinear set of coupled equations in Eqs. (61) to (63) is linearised to solve using an incremental iterative technique. For this, the solution at the current iteration $k+1$ is approximated using the Taylor series expansion around the solution of the previous iteration k neglecting the quadratic and higher order terms, i.e.,

$$\begin{aligned}
\mathbf{R}_{\boldsymbol{\varphi}}(\boldsymbol{\varphi}^{k+1}, p^{k+1}, \phi^{k+1}) &\approx \mathbf{R}_{\boldsymbol{\varphi}}(\boldsymbol{\varphi}^k, p^k, \phi^k) + \mathrm{D}\mathbf{R}_{\boldsymbol{\varphi}}(\boldsymbol{\varphi}^k, p^k, \phi^k)[\delta\boldsymbol{\varphi}] + \mathrm{D}\mathbf{R}_{\boldsymbol{\varphi}}(\boldsymbol{\varphi}^k, p^k, \phi^k)[\delta p] \\
&\quad + \mathrm{D}\mathbf{R}_{\boldsymbol{\varphi}}(\boldsymbol{\varphi}^k, p^k, \phi^k)[\delta\phi] = \mathbf{0} \\
\mathbf{R}_p(\boldsymbol{\varphi}^{k+1}, p^{k+1}, \phi^{k+1}) &\approx \mathbf{R}_p(\boldsymbol{\varphi}^k, p^k, \phi^k) + \mathrm{D}\mathbf{R}_p(\boldsymbol{\varphi}^k, p^k, \phi^k)[\delta\boldsymbol{\varphi}] + \mathrm{D}\mathbf{R}_p(\boldsymbol{\varphi}^k, p^k, \phi^k)[\delta p] \\
&\quad + \mathrm{D}\mathbf{R}_p(\boldsymbol{\varphi}^k, p^k, \phi^k)[\delta\phi] = \mathbf{0} \\
\mathbf{R}_\phi(\boldsymbol{\varphi}^{k+1}, p^{k+1}, \phi^{k+1}) &\approx \mathbf{R}_\phi(\boldsymbol{\varphi}^k, p^k, \phi^k) + \mathrm{D}\mathbf{R}_\phi(\boldsymbol{\varphi}^k, p^k, \phi^k)[\delta\boldsymbol{\varphi}] + \mathrm{D}\mathbf{R}_\phi(\boldsymbol{\varphi}^k, p^k, \phi^k)[\delta p] \\
&\quad + \mathrm{D}\mathbf{R}_\phi(\boldsymbol{\varphi}^k, p^k, \phi^k)[\delta\phi] = \mathbf{0}
\end{aligned} \tag{64}$$

This results in a fully coupled system of linear equations which can be written in the following form:

$$\begin{bmatrix} \mathbf{K}_{\varphi\varphi} & \mathbf{K}_{\varphi p} & \mathbf{K}_{\varphi\phi} \\ \mathbf{K}_{p\varphi} & \mathbf{K}_{pp} & \mathbf{K}_{p\phi} \\ \mathbf{K}_{\phi\varphi} & \mathbf{K}_{\phi p} & \mathbf{K}_{\phi\phi} \end{bmatrix} \begin{bmatrix} \Delta\boldsymbol{\varphi} \\ \Delta p \\ \Delta\phi \end{bmatrix} = - \begin{bmatrix} \mathbf{R}_{\varphi} \\ \mathbf{R}_{p} \\ \mathbf{R}_{\phi} \end{bmatrix} \tag{65}$$

The Newton iterations for the above monolithic solver often fails to converge because of the non-convexity of the total potential energy functional with respect to the field variables [111]. As a result staggard/alternating minimisers are popular among the phase field community wherein, the displacement and damage field variables are solved sequentially. However, the later suffers from the lack of unconditional stability and requires small time increments resulting in an extremely slow solution. Hence numerous attempts have been made in the past to employ monolithic solvers for phase field problems [112–115]. Wu et al. [116] demonstrated the effectiveness of the quasi-Newton monolithic approach to solve phase field problem. Later, Kristensen and Pañeda [117] demonstrated that a BFGS based monolithic solver with the help of an adaptive time stepping scheme results in up to 100 times reduction in the computing time as compared to that of the staggered scheme. Hence in the present study, we employ a quasi-Newton based monolithic scheme to solve the coupled displacement–damage problem. The set of nonlinear equations in Eq. (64) can be written as

$$\mathbf{R}^{k+1} - \mathbf{R}^{k} = \mathbf{K}^{k}[\mathbf{a}^{k+1} - \mathbf{a}^{k}] \tag{66}$$

where, $k+1$ is the current iteration, the residual vector $\mathbf{R} = [\mathbf{R}_{\boldsymbol{\varphi}}\ \mathbf{R}_{p}\ \mathbf{R}_{\phi}]^{T}$ and the vector of field variables $\mathbf{a} = [\boldsymbol{\varphi}\ p\ \phi]^{T}$. Now for a quasi-Newton method, the stiffness matrix $\mathbf{K}$ is substituted with an approximation $\widetilde{\mathbf{K}}$ satisfying the secant condition:

$$\delta\mathbf{R} = \widetilde{\mathbf{K}}\delta\mathbf{a} \tag{67}$$

where, $\delta\mathbf{R} = \mathbf{R}^{k+1} - \mathbf{R}^{k}$ and $\delta\mathbf{a} = \mathbf{a}^{k+1} - \mathbf{a}^{k}$. Now the approximated $\widetilde{\mathbf{K}}$ in the current iteration is found from

$$\widetilde{\mathbf{K}} = \widetilde{\mathbf{K}}^{k} - \frac{[\widetilde{\mathbf{K}}^{k}\delta\mathbf{a}][\widetilde{\mathbf{K}}^{k}\delta\mathbf{a}]^{T}}{\delta\mathbf{a}^{T}\widetilde{\mathbf{K}}^{k}\delta\mathbf{a}} + \frac{\delta\mathbf{R}\delta\mathbf{R}^{T}}{\delta\mathbf{R}^{T}\delta\mathbf{R}} \tag{68}$$

However, Matthies and Strang [118] proposed to calculate the inverse of the approximated symmetric stiffness matrix as

$$\widetilde{\mathbf{K}}^{-1} = \left[\mathbf{I} - \frac{\delta\mathbf{a}\delta\mathbf{R}^{T}}{\delta\mathbf{a}^{T}\delta\mathbf{R}}\right]\left[\widetilde{\mathbf{K}}^{(k)}\right]^{-1}\left[\mathbf{I} - \frac{\delta\mathbf{a}\delta\mathbf{R}^{T}}{\delta\mathbf{a}^{T}\delta\mathbf{R}}\right]^{T} + \frac{\delta\mathbf{a}\delta\mathbf{R}^{T}}{\delta\mathbf{a}^{T}\delta\mathbf{R}} \tag{69}$$

which proves to be computationally efficient as it involves only the inner products of vectors and its scaling. Now looking back at the linearisation in Eq. (65), it can be observed that the Jacobian matrix is not symmetric as $\mathbf{K}_{\varphi\phi} \neq \mathbf{K}_{\phi\varphi}^{T}$ and $\mathbf{K}_{p\phi} \neq \mathbf{K}_{\phi p}^{T}$ due to the presence of history fields $\mathcal{H}_1$ and $\mathcal{H}_2$. Hence a weak coupling is assumed such that $\mathbf{K}_{\varphi\phi} = \mathbf{0}$, $\mathbf{K}_{p\phi} = \mathbf{0}$, $\mathbf{K}_{\phi\varphi} = \mathbf{0}$, $\mathbf{K}_{\phi p} = \mathbf{0}$ resulting in the following system of equations with symmetry.

$$\begin{bmatrix} \mathbf{K}_{\varphi\varphi} & \mathbf{K}_{\varphi p} & \mathbf{0} \\ \mathbf{K}_{p\varphi} & \mathbf{K}_{pp} & \mathbf{0} \\ \mathbf{0} & \mathbf{0} & \mathbf{K}_{\phi\phi} \end{bmatrix} \begin{bmatrix} \Delta\boldsymbol{\varphi} \\ \Delta p \\ \Delta\phi \end{bmatrix} = - \begin{bmatrix} \mathbf{R}_{\varphi} \\ \mathbf{R}_{p} \\ \mathbf{R}_{\phi} \end{bmatrix} \tag{70}$$

where,

$$\mathbf{K}_{\varphi\varphi} = \frac{\partial\mathbf{R}_{\varphi}}{\partial\boldsymbol{\varphi}} = \int_{\Omega} \mathbf{G}_{\varphi}^{T}\, \mathbb{e}\, \mathbf{G}_{\varphi}\, \mathrm{d}v \tag{71}$$

$$\mathbf{K}_{\varphi p} = \frac{\partial\mathbf{R}_{\varphi}}{\partial p} = \int_{\Omega} \mathbf{D}_{\varphi}^{T}\mathbf{N}_{p}\, \mathrm{d}v = \mathbf{K}_{p\varphi}^{T} \tag{72}$$

$$\mathbf{K}_{pp} = \frac{\partial\mathbf{R}_{p}}{\partial p} = -\int_{\Omega_0} \frac{1}{K}\mathbf{N}_{p}^{T}\mathbf{N}_{p}\, \mathrm{d}V \tag{73}$$

$$\begin{aligned} \mathbf{K}_{\phi\phi} = \frac{\partial\mathbf{R}_{\phi}}{\partial\phi} = \int_{\Omega_0} \Big[& -G_c l \mathbf{B}_{\phi}^{T}\boldsymbol{B}_{\phi} - \frac{G_c}{l}\mathbf{N}_{\phi}^{T}\mathbf{N}_{\phi} \\ & + 2\mathbf{N}_{\phi}^{T}\mathbf{N}_{\phi}\mathcal{H}_1 + 6\mathbf{N}_{\phi}^{T}\mathbf{N}_{\phi}[1-\phi]p\mathcal{H}_2 + \frac{\eta}{\Delta t}\mathbf{N}_{\phi}^{T}\mathbf{N}_{\phi} \Big]\, \mathrm{d}V \end{aligned} \tag{74}$$

The fourth order material tangent tensor $\mathbb{e}$ is defined by

$$e_{ijkl} = g(\phi)\frac{1}{J}F_{jJ}\frac{\partial P_{iJ}}{\partial F_{kL}}F_{lL} + f(\phi)p[\delta_{ij}\delta_{kl} - \delta_{il}\delta_{jk}] \tag{75}$$

It is worth noting that both the mechanical and damage components of the Jacobian matrix are symmetric and positive definite. Hence the BFGS approximation of the Jacobian $\widetilde{\mathbf{K}}$ is also symmetric and positive definite making the monolithic scheme admissible. The numerical framework established in this section is implemented in the commercial finite element software ABAQUS with the help of a User Defined Element(UEL) subroutine. The elemental stiffness matrix and the residuals calculated here are defined in the UEL subroutine, which later is used by ABAQUS to generate the global stiffness matrix and the residual vectors. The Gauss quadrature rule is used to approximate the integrals at the element level. Further, the UEL subroutine is developed in a thread safe manner to use the parallel processing capability of ABAQUS. The three field problem is solved using a monolithic solver utilising the inbuilt BFGS technique of ABAQUS. Finally, the numerical simulations are run using the HP EliteDesk 800 G6 Tower desktop utilising the Intel® Core™ i7-10700 processor having eight cores.

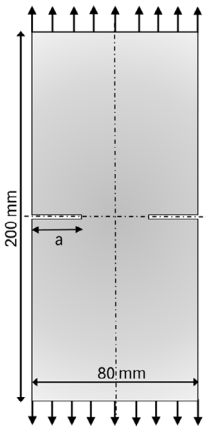

(a) Full geometry

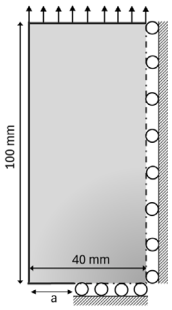

(b) Domain and boundary conditions considered in the simulation due to symmetry.

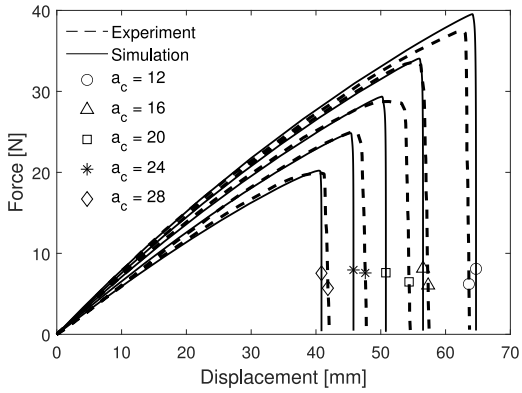

(c) load-displacement curves for different values of initial pre-crack compared with that of experiments by Hocine et al. [119]

Fig. 4. Double edged notch tensile specimen with different pre-crack length 'a'. Utilising the symmetry of the specimen, only one-eighth portion of the domain is discretised. Further, the results of the simulation are compared to that of experiments conducted by Hocine et al. [119] for five different pre-crack lengths $a \in [12, 16, 20, 24, 28]$ mm.

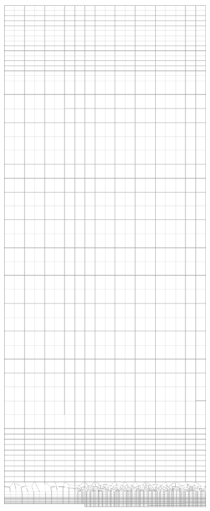

Fig. 5. Mesh used for double edged notch tensile test sample with $a = 16$ mm. A finer element size of 0.2 mm is used in the area of crack propagation.

4. Numerical examples

In this section, we apply the proposed mixed displacement–pressure–damage formulation to three fracture problems each dealing with a separate constraint in damage modelling. The first investigation is that of a standard double edge slit problem comparing the results with that of experiments. The second problem is an out-of plane tearing of a membrane sheet illustrating the capability of the method to predict damage at very high stretch levels. Lastly, we look at a 3D printed polymer sample with rigid inclusions where fracture initiates and propagates at multiple locations within the same sample.

4.1. Example one: Double edged notch

Fracture tests on double edged notch specimen is a common example used by the computational community to illustrate the performance of a numerical framework. The work is based on experiments conducted by Hocine et al. [119] on a rectangle specimen with pre-cracks of different lengths at the centre of the specimen on either edges. The results are presented in terms of load–displacement curves illustrating a sharp reduction in load carrying capacity as the fracture propagates. The experiment consists of thin rectangle sheets made of styrene–butadiene rubber (SBR) of size 200 mm × 80 mm × 3 mm as shown in Fig. 4(a). Five different pre-crack lengths $a = [12, 16, 20, 24, 28]$ mm where considered in the study. Taking advantage of the symmetry of the specimen, 1/8th of the domain is modelled using symmetry boundary conditions are shown in Fig. 4(b). The FEM discretisation is performed using

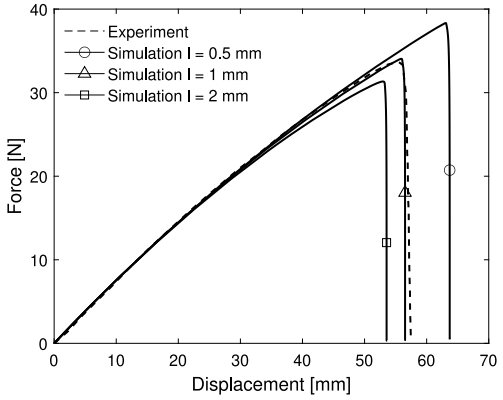

Fig. 6. Load–displacement curve for double edged notch specimen having 16 mm precrack length corresponding to three different lengthscale parameters $l \in [0.5,\ 1,\ 2]$ mm.

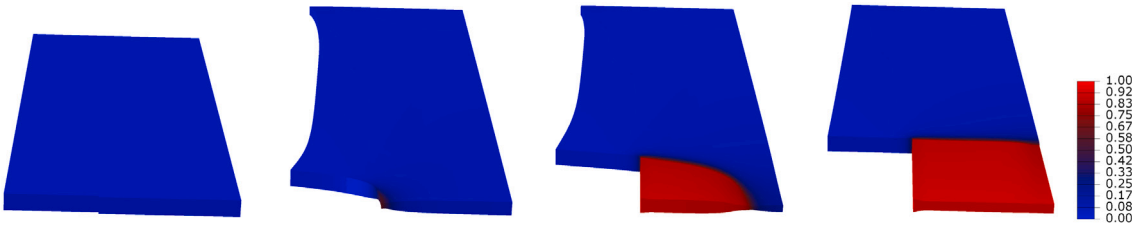

(a) u=0.0 mm (b) u=56.06 mm (c) u=56.52 mm (d) u=56.52 mm

Fig. 7. Damage contour $[\phi]$ depicting the state of fully damaged material at different instants of loading for $a_c = 16$ mm. Throughout the work, damage contour plots are represented using the same colour scheme and henceforth the legends are omitted in the upcoming fracture plots. (For interpretation of the references to colour in this figure legend, the reader is referred to the web version of this article.)

Table 1
Material properties used for double edged notch specimen.

μ	ν	K	η	G_c	l	ϵ
0.2415 MPa	0.499	120.67 MPa	0.001 MPa s	2.88 N mm^{-1}	1.0 mm	0.0002

3D Q1Q0Q1 brick elements having 33dofs each. A nonuniform mesh of 28,000 elements with finer elements of the size of $l/5$ was chosen in the area of expected crack propagation as shown in Fig. 5. Fig. 6 represents the load–displacement plots for a pre-crack length of 16 mm corresponding to three different lengthscale parameters 0.5 mm, 1 mm and 2 mm. Overall, it can be seen that the peak load and displacement increases with a decrease in the lengthscale parameter. For the simulation, the lengthscale parameter is chosen as $l = 1$ mm similar to that of Miehe and Schänzel [42] and a critical fracture energy $G_c = 2.88$ N/mm is considered based on the calibration of the model for $a = 16$ mm. The artificial viscous stabilisation η parameter was chosen to be 0.001 and the elastic properties, shear modulus $\mu = 0.2415$ MPa and Poison's ratio $\nu = 0.499$ giving rise to an initial bulk modulus $K = 120.67$ MPa the material properties used in the simulation are summarised in the Table 1. Fig. 4(c) represents the load–displacement plots where the solid lines and broken line represents the results from numerical and experimental study, respectively. The fracture parameters are calibrated against $a = 16$mm and are adopted for the rest of the cases. Overall, the numerical models follows the experimental results capturing the peak load and failure stretch in all five cases.

Fig. 7 illustrates the contour plot for the damage $[\phi]$ at different vertical displacement values. The effect of the incompressibility is evident from the out of plane compression of the elements at the location of stress concentration. However, the incompressibility constraint gets relaxed at advanced stages of damage due to the use of appropriate $f(\phi)$ and $g(\phi)$. As a result, the elements undergo significant volume change to attain a relaxed configuration as shown in Figs. 7(c) and 7(d). This approach enables the stable propagation of crack by alleviating any difficulties due to warped and twisted elements at advanced stages of damage. Further, the damaged elements do not have any physical relevance as they carry negligible stresses in the simulation and can be safely ignored [49,87]. Fig. 8 illustrates the crack opening and its propagation at different stages of loading. Fig. 8(b) corresponds to the peak load of the specimen where the displacement has reached 56.06 mm and the crack continues to propagate until the full fracture at around 56.52 mm as shown in Fig. 8(e). The intermediate stages of the crack propagation are illustrated in Figs. 8(c) and 8(d) corresponding to 56.50 mm and 56.52 mm displacements, respectively. Further, Fig. 9 shows the contour plots for the Cauchy stress component $[\sigma_{22}]$ at different stages of the loading. At the peak loading condition, the vertical component of the stress at the crack tip reads at 1.21 MPa as shown in Fig. 9(a) which thereafter increases steadily as crack propagates to reach a peak value of 7.20

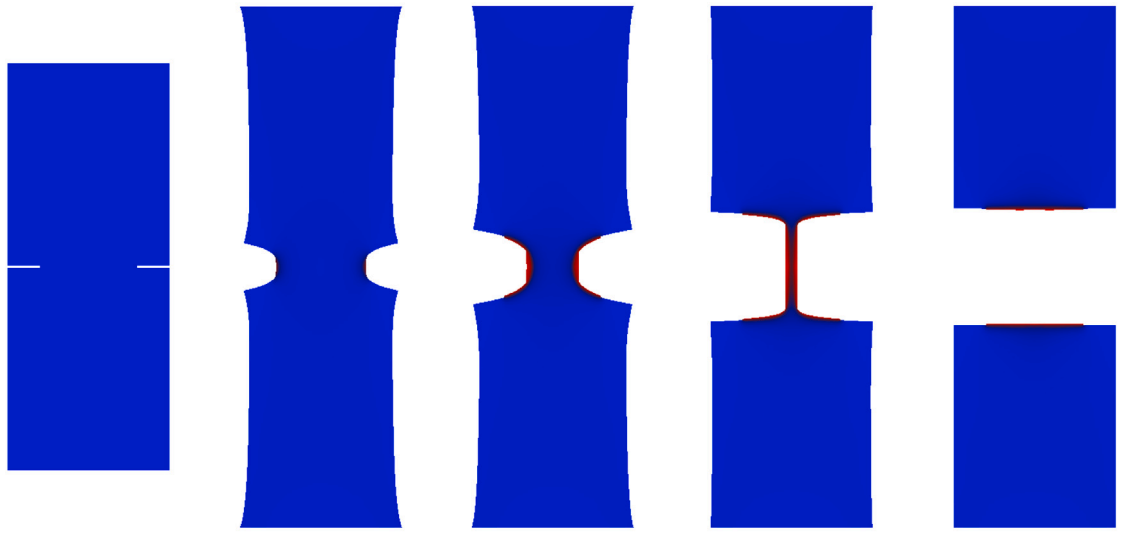

(a) u=0.0 mm (b) u=56.06 mm (c) u=56.50 mm (d) u=56.52 mm (e) u=56.52 mm

Fig. 8. Damage contour [ϕ] plot for the double edged notch specimen having $a = 16$ mm. The crack initiates at the tip of the pre-crack and propagates to the centre of the specimen. To visualise the crack opening, all elements having $\phi > 0.85$ are removed here.

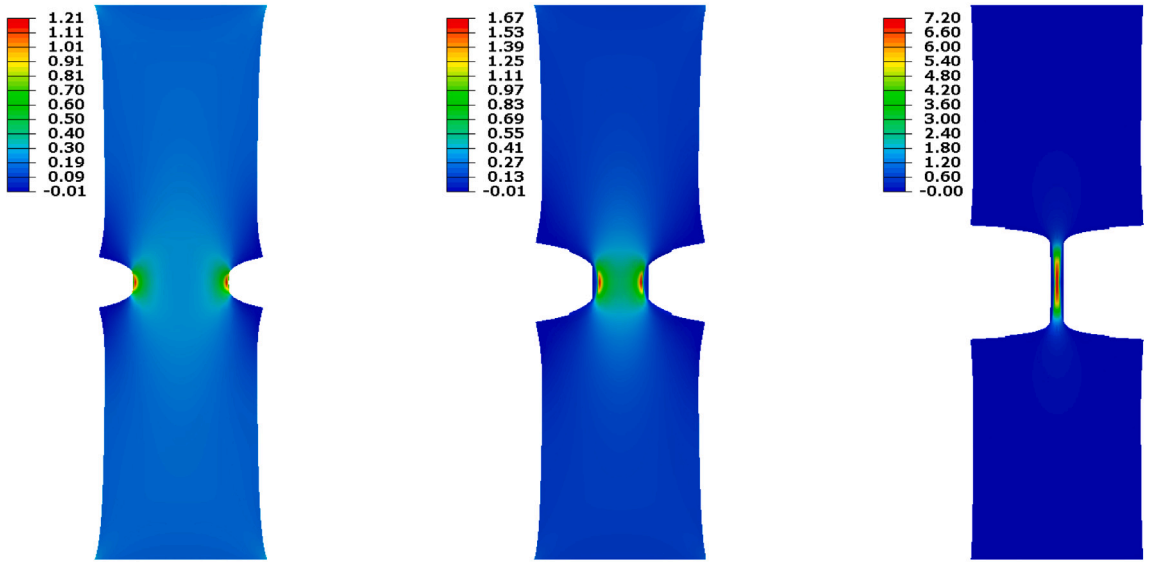

(a) u=56.06 mm (b) u=56.50 mm (c) u=56.52 mm

Fig. 9. Visualisation of the vertical component of the Cauchy stress [MPa] at different instances of loading. To visualise the crack opening, all elements having $\phi > 0.85$ are removed here.

MPa just before full fracture Fig. 9(c). The pressure [p] contour plots shown in Fig. 10 also shows a similar behaviour where in the pressure value of 0.41 MPa at the start of the crack propagation reaches a peak value of 2.35 MPa just before the full fracture. It is also important to note that the overall pressure contribution to the Cauchy stress stands roughly at 33% throughout the fracture process.

4.2. Example two: Out of plane tearing

In this example, we consider a rubber sheet of 48 mm length, 36 mm wide, and 0.5 mm thick with a pre-crack of 12 mm. To conduct the out of plane tearing test, we assume that a half width of the sheet is clamped by sandwiching between two rigid plates.

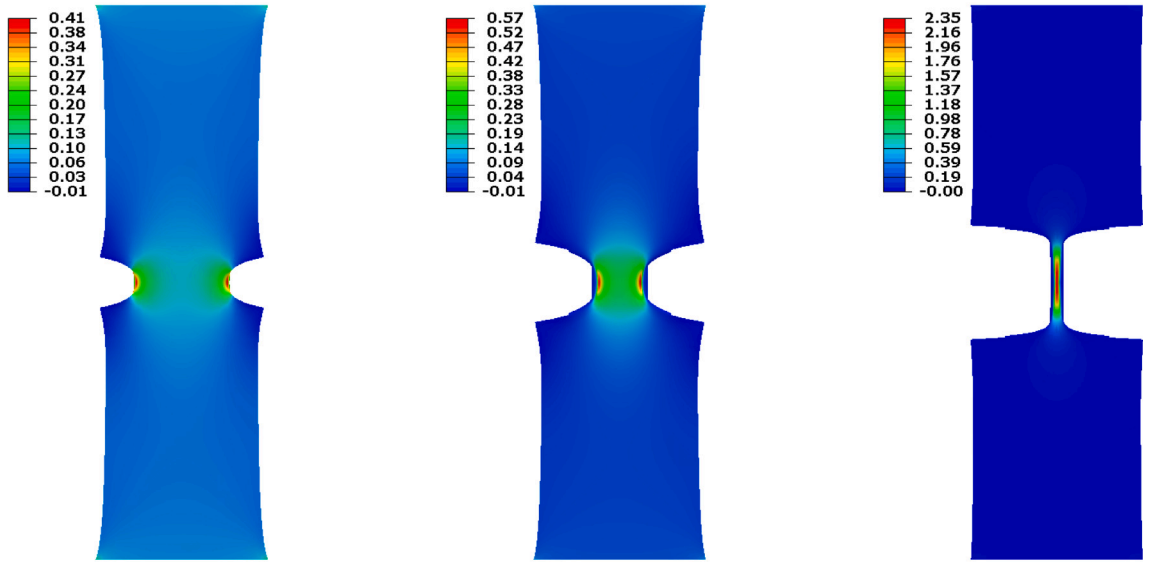

(a) u=56.06 mm (b) u=56.50 mm (c) u=56.52 mm

Fig. 10. Visualisation of the pressure component [MPa] of the Cauchy stress at different instances of loading. To visualise the crack opening, all elements having $\phi > 0.85$ are removed here.

Table 2
Material properties used for out of plane tear test.

μ	ν	K	η	G_c	l	ϵ
0.203 MPa	0.499	101.43 MPa	0.001 MPa s	0.35 N mm^{-1}	0.5 mm	0.0002

Hence, the simulations are done by taking into account only a half width of the specimen by assuming rigid boundary conditions at one edge as shown in Fig. 11(a). A vertical displacement is given to the edge closer to the pre-crack such that crack propagation happens along the clamped edge. X - displacements are arrested along the edge of loading to simulate the clamping effect at the loading edge. Similar to the previous case, 3D Q1Q0Q1 brick elements are used in the simulations. The elements sizes are refined to around l/5 in the zone of crack propagation resulting in a total of 11,139 elements. The length scale parameter is set to 0.5 mm and critical fracture energy is taken as 0.35 N/mm. The constitutive parameters chosen for the simulation is summarised in Table 2.

Fig. 11(c) represents the force vs. displacement curve for the numerical experiment conducted. Peak loading occurs at a vertical displacement of $u \approx 14.8$ mm and crack starts to propagate drastically resulting in a slight reduction in applied load which later stabilises at around 0.1 N and stays constant as the tearing propagates through the restrained edge. Further, the force drops drastically as the crack path reaches the end of the specimen at around $u \approx 50$ mm vertical displacement. Fig. 12 illustrates the damage contour plot corresponding to different instances of loading. The sheet undergoes elastic loading until $u \approx 14$ mm and crack initiates at the tip of the initial notch. Further, the crack propagates steadily until the full rupture of the specimen occurs at around $u \approx 50.33$ mm. It is also meaningful to look the stress and pressure contours from the numerical experiment and is represented at an intermediate loading state in Fig. 13. Fig. 13(a) represents the vertical displacement contour showing the maximum value at the loading edge. Further, Figs. 13(b) and 13(c) illustrates the Cauchy stress component [σ_{22}] and pressure [p] at $u \approx 40.5$ mm, where the stress concentration ahead of the crack propagation can be seen. Contrary to the previous numerical example, the present case yields a negative value for minimum stress and pressure components. This is due to the out of plane nature of loading wherein, the top face ahead of the crack tip is constantly in a compressive state due to the bending action.

4.3. Example three: Composite samples with rigid inclusions

This example stems from a series of experiments conducted by Russ et al. [78], where a soft elastomer (TangoBlackPlus) is 3D printed with three circular rigid inclusions of VeroWhite material. The study consisted of nine specimens with three different inclusion's spacings and initial notch length. The rectangular specimens are of 48 mm long and 24 mm wide with 2.5 mm thickness. A schematic of the specimen is illustrated in Fig. 14 wherein the samples are named based on the distance between the inclusions and the pre-cut length. Here, the name NxxDyy means the 'xx'% of width for initial notch length and 'yy'mm for the distance between the inclusions. The material properties used for the numerical simulation are reported in Table 3 where larger values are assumed for the phase field related properties of the rigid inclusions as the damage is expected in the soft TP material. The symmetry of the

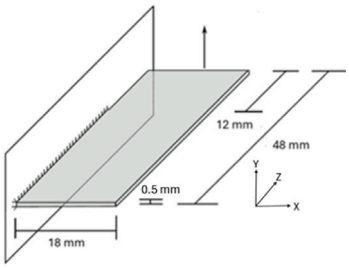

(a) Domain and boundary conditions considered for the out of plane tearing test.

(b) Mesh used for simulation.

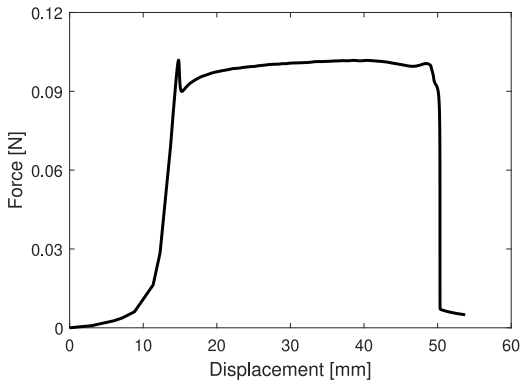

(c) Load-displacement curve

Fig. 11. Out of plane tearing test: A rectangular sheet of 48 mm × 18 mm × 0.5 mm is assumed to be clamped for a length of 36 mm along one edge as shown in Fig. 11(a). A pre-crack of 12 mm is included by providing a free boundary condition along the clamped edge. The loading edge is pulled vertically until the sheet fully tears at the clamped edge and the reaction force is identified as the tearing force for the numerical experiment. Fig. 11(b) illustrates the mesh used for the simulation where a finer element size of 0.1 mm is used in the region of crack propagation. The tearing force–displacement plot is shown in Fig. 11(c).

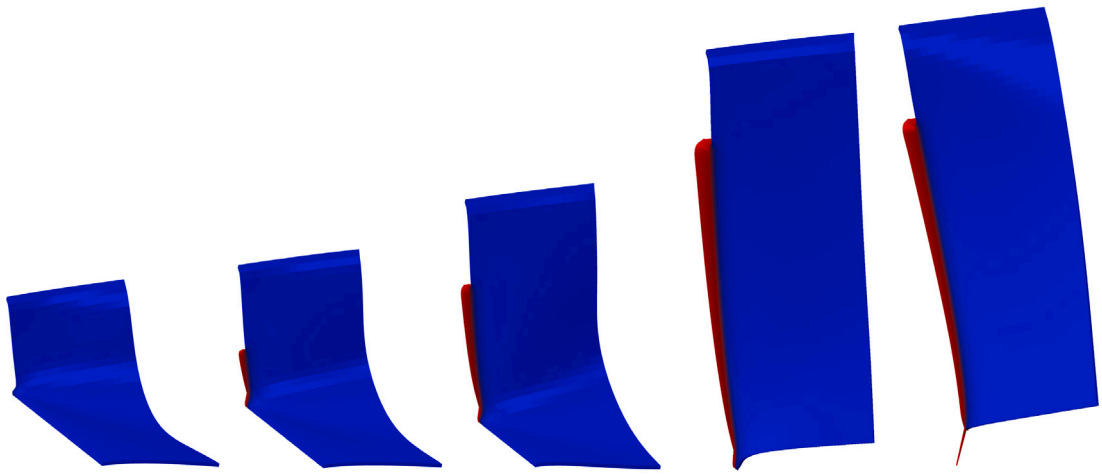

(a) $u \approx 13.7$ mm (b) $u \approx 20$ mm (c) $u \approx 30$ mm (d) $u \approx 50.23$ mm (e) $u \approx 50.33$ mm

Fig. 12. Damage contour [ϕ] plot for the out of plane tearing experiment at different intervals of displacement loading. To visualise the crack opening, all elements having $\phi > 0.85$ are removed here.

model about the horizontal axis is preserved however, the centre rigid inclusion is perturbed by 0.024 mm to match the fracture behaviour from the experiments and is in line with procedure reported in [78] and later by [49]. This is done to match the crack propagation observed from experiments. Fig. 15 illustrates the crack path and load–displacement behaviour of N10D18 sample using a symmetric geometry for simulation. The symmetric assumption resulted in the formation of cracks on either side of the central inclusion. Consequently, the load–displacement curve shows a stiffening behaviour in post peak regime. The shear modulus of the soft elastomer is taken as $\mu = 0.25$ MPa and the Poison's ratio is assumed to 0.499 resulting in a bulk modulus of $K = 100$ MPa. The numerical stability parameter $\eta = 0.0001$ MPa s is chosen so that it has minimal influence on the response of the specimen. Further, the damage parameters are calibrated against the response of N10D24 sample. A fine mesh of size $h = l/4$ is chosen in the regions of expected crack propagation for all the samples as shown in Fig. 16.

The load–displacement results are plotted in Fig. 17 and is compared with the experimental results from Russ et al. [78]. Further, the crack paths for a total of five cases as originally reported by Russ et al. [78] is illustrated in Figs. 18, 19 and 20. Overall, there are two possible cases for the location of crack initiation, firstly at the pre-crack tip and secondly in-between the central rigid inclusions depending on the geometry of the specimen. For instance, the case of D30 specimens, all three samples initiate crack from the

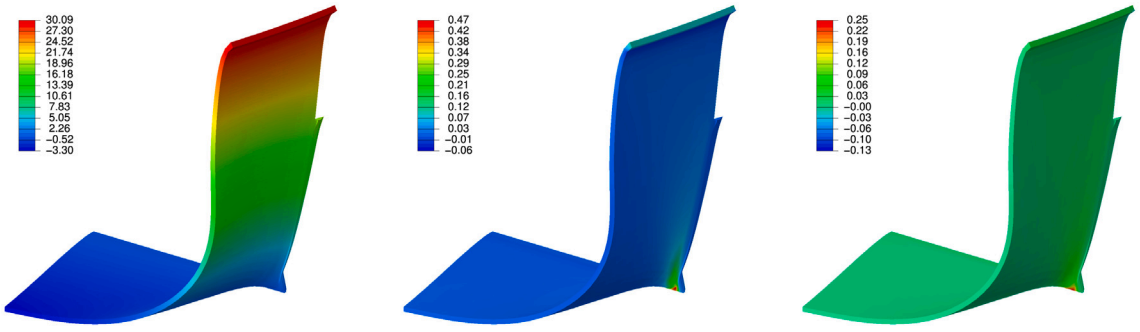

(a) Vertical displacement contour at $u \approx 40.5$ mm.

(b) Component of Cauchy stress $[\sigma_{22}]$ plot at $u \approx 40.5$ mm. [unit - MPa]

(c) Contour plot of pressure [p] at $u \approx 40.5$ mm. [unit - MPa]

Fig. 13. Out of plane tearing experiment: Contour plots of different quantities at a vertical displacement of $u \approx 40.5$ mm. Stress concentration ahead of the crack path can be seen in the contour plots of both $[\sigma_{22}]$ and [p]. To visualise the crack opening, all elements having $\phi > 0.85$ are removed here.

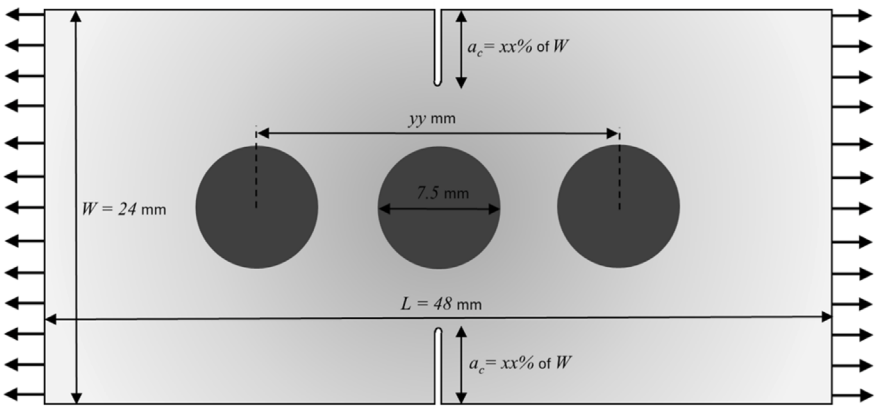

Fig. 14. Sketch showing the geometry of the 48 mm long, 24 mm wide and 2.5 mm thick rectangular polymer sample with 7.5 mm diameter rigid inclusions. Initial pre-crack length $a_c = xx\%$ of W and the distance between the inclusions $d = yy$ mm such that the corresponding specimens are named as NxxDyy.

Table 3
Material properties used for the composite sample with rigid inclusions.

Material	μ [MPa]	ν	K [MPa]	η	G_c	l [mm]	ϵ_{res}
TP	0.25	0.499	100	0.0001	0.79	0.2	0.002
VW	714	0.4	333.3	0.0001	1	1	0.002

pre-crack tip and propagates until it reaches the central inclusions. Fig. 18 illustrates a comparison of the crack path obtained from numerical simulation and experiment for the cases of N05D30 and N20D30 specimens. For both the cases, as the crack path reaches the central inclusion, a secondary crack initiates in-between the space of the inclusions close to the central one and propagates until it meets the primary crack. However, the experimental result for N05D30 shows two secondary cracks developed on either side of the central inclusion, but on further loading, the one on the left becomes critical and leads to complete failure. The simulation also follows a similar fashion where the damage value on each side reaches around 40% before the damage on the left side becomes critical and leads to crack propagation. The behaviour for N20D30 sample is slightly different where the experimental results show only a secondary crack formation on the right side and is replicated in the simulation where the damage values on the left side stays at around 25%. A similar behaviour is also shown by N10D30 sample where the damage value on the non propagating side saturates at around 28% before the other side becomes critical. Fig. 17(c) represents the load–displacement plots for the three pre-crack lengths for D30 specimens. N05D30 specimen shows good agreement in the failure load as well as failure stretch, however, the stiffening of the sample post the primary crack propagation is missed here. As a result, the stretch value at which both the cracks propagate is the same and is around 1.4921, whereas the experimental results show stretch values of 1.3854 and 1.4931 for primary and secondary crack propagation, respectively. But for the case of N20D30 specimen, the numerical simulation is able to capture the gap between the stretch values of primary crack saturation and secondary crack initiation even though the values does not match exactly with experiments. However, the simulation slightly under predicts the failure force. A similar fashion is also observed by the numerical results from Russ et al. [78] however, their model underpredicts both the values of critical stretch and load to the

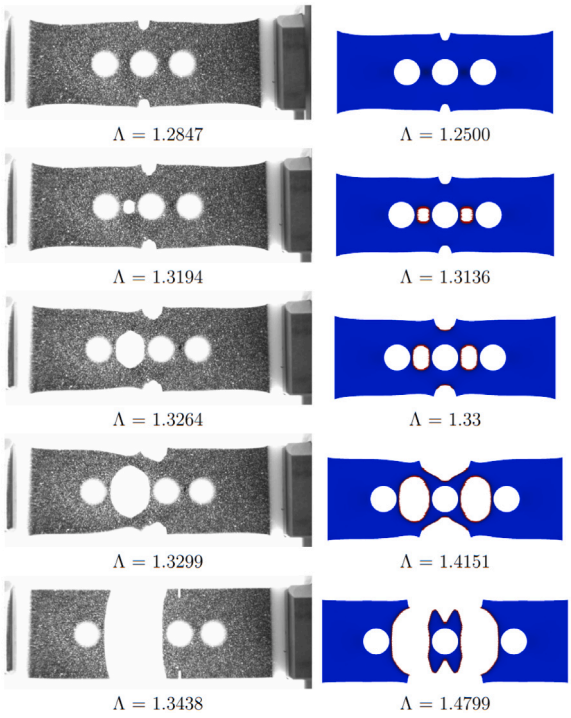

(a) Damage Contour plots [ϕ] of N10D18 sample assuming symmetry.

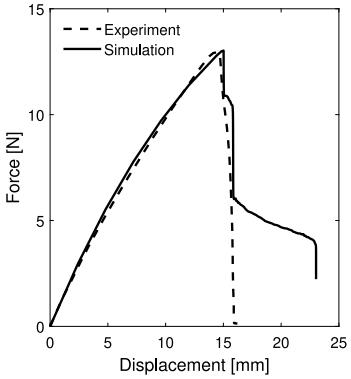

(b) Load Displacement plot of N10D18 sample assuming symmetry.

Fig. 15. The results of the simulation assuming symmetry of the sample about the horizontal and vertical axes. A comparison of the crack path is provided in (a), where the images on the left shows the experimental results [78] and the images on the right shows simulation results. To visualise the crack paths, all elements having $\phi > 0.85$ are removed here. The load–displacement plots from the experiments and simulation are illustrated in (b).

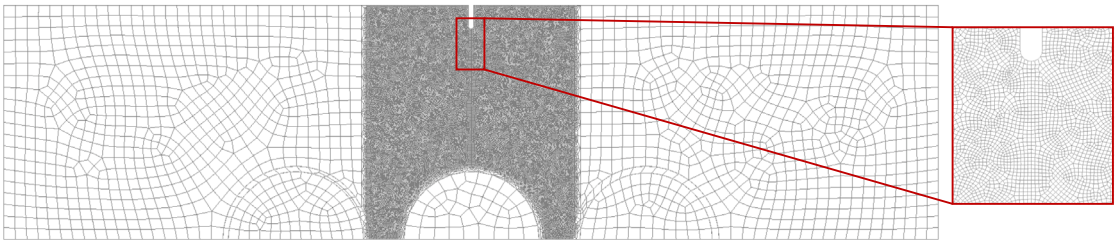

Fig. 16. Mesh used for N10D18 specimen, where a minimum element size of 0.05 mm was used in the area of crack propagation. This resulted in a total of 150,735 Q1Q0Q1 elements.

extend that the failure stretches of the N05 and N20 samples are equal which is not the case from experiments. This could be due to the fact that the simulations use a 2D assumptions and the phase field model is based on the critical energy criterion proposed by Miehe et al. [120]. The implementation of Arunachala et al. [49] which is based on 3D elements and a micromechanically motivated constitutive model greatly improves the overall behaviour, however, the current implementation yields better results for the N05 sample. In the case of D18, samples develop crack at the location between the central inclusions. This can be observed in both the experimental and simulation results of crack path illustrated in Fig. 19 for N10D18 and N05D18 samples. For N05D18 sample, the crack initiates in-between the central inclusions and propagate outwards to the border of the sample for both the simulation and experiment. The small pre-crack introduced does not develop into a crack initiation as the maximum value of damage at the notch tip is saturated at roughly 30%. However, for the case of N10 sample, as the crack propagates from the centre of the sample, the simulation shows a secondary crack initiation at the notch tip similar to that shown from the experiments. But the crack path originating from the notch tip fails to meet the primary crack as it continues to develop in the direction of the sample edge. Note that both the implementations of Russ et al. [78] and Arunachala et al. [49] fail to capture this as their primary crack path deviates its initial direction to meet the secondary crack originating from the notch tip. The load–displacement curves for the D18 samples are plotted in Fig. 17(a), where there is a good agreement between the experimental and simulation results for the N20 sample. For the case of N10 sample, even though the failure stretches agree well, the simulation slightly underpredicts the peak load. The

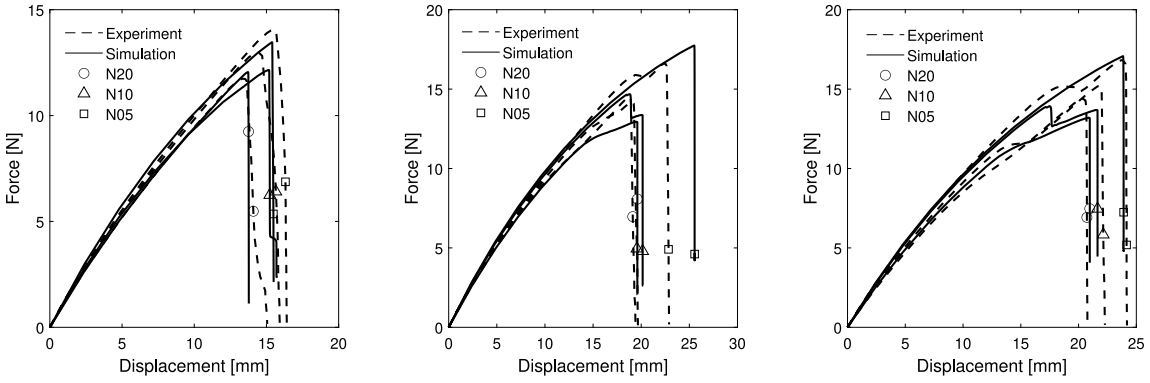

Fig. 17. Load–displacement plots comparing the results from experiments and numerical study. The results of experiments are taken from the study of Russ et al. [78].

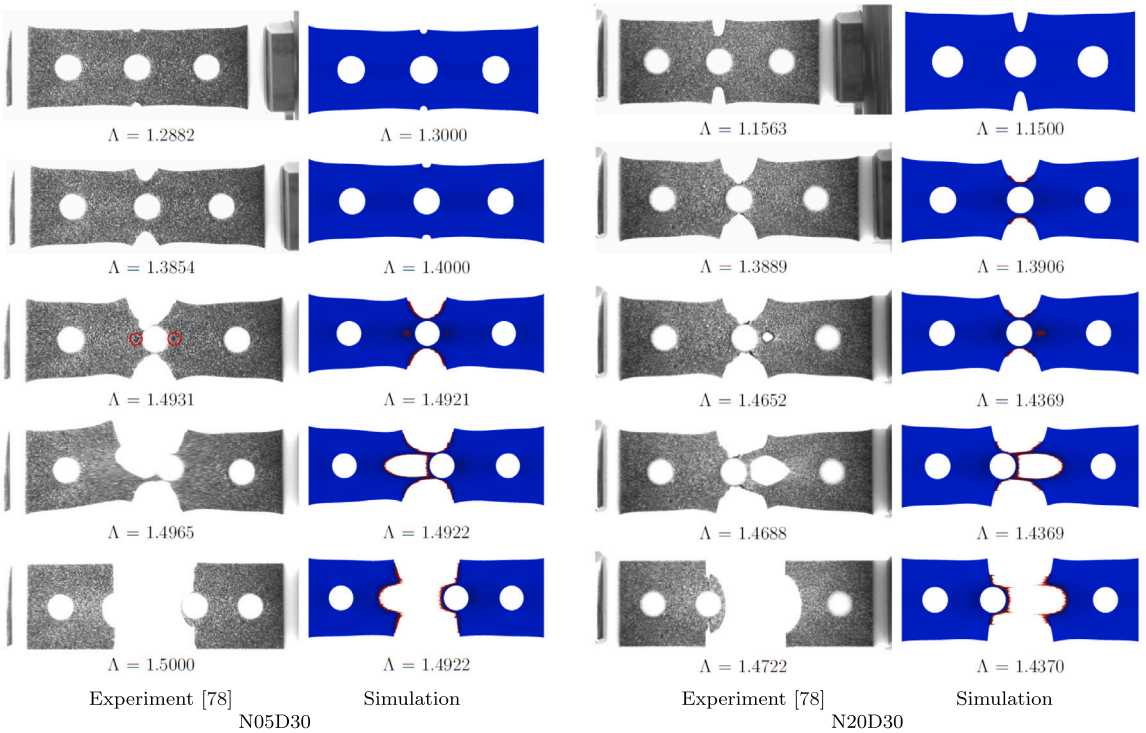

Fig. 18. Damage contour [ϕ] plots showing the crack initiation and propagation paths for different values of global stretch Λ compared to that of experiments conducted by Russ et al. [78]. Two specimen geometries namely N05D30 and N20D30 are compared here. To visualise the crack paths, all elements having $\phi > 0.85$ are removed here.

N05 sample shows a better prediction for both the peak load and failure stretches, however, the slope of the post peak zone is not reflected in the simulation. This can be better captured by using a higher value of the numerical damping parameter η as shown by Arunachala et al. [49].

Finally, Fig. 20 shows the crack for the N20D24 sample, where the crack initiates at the pre-crack tip and travels to the interior of the sample. Once the primary crack reaches the central inclusion, a secondary crack is initiated on the left side of the central inclusion and it propagates in a direction to meet the primary crack for a full failure. The crack paths of both the experiment and simulations match well. Fig. 17(b) represents the load–displacement plots for D24 samples. The prediction of N10 sample matches reasonably well with that of the experiment. For the case of N20 the slope of the curve reduces at a higher rate than that of the experiments while damage accumulates at the notch tip resulting in a lower failure load. However, for the N05 sample, the slope of the curve matches well with that of experiments, but the failure stretch and the peak load are over predicted. A similar behaviour

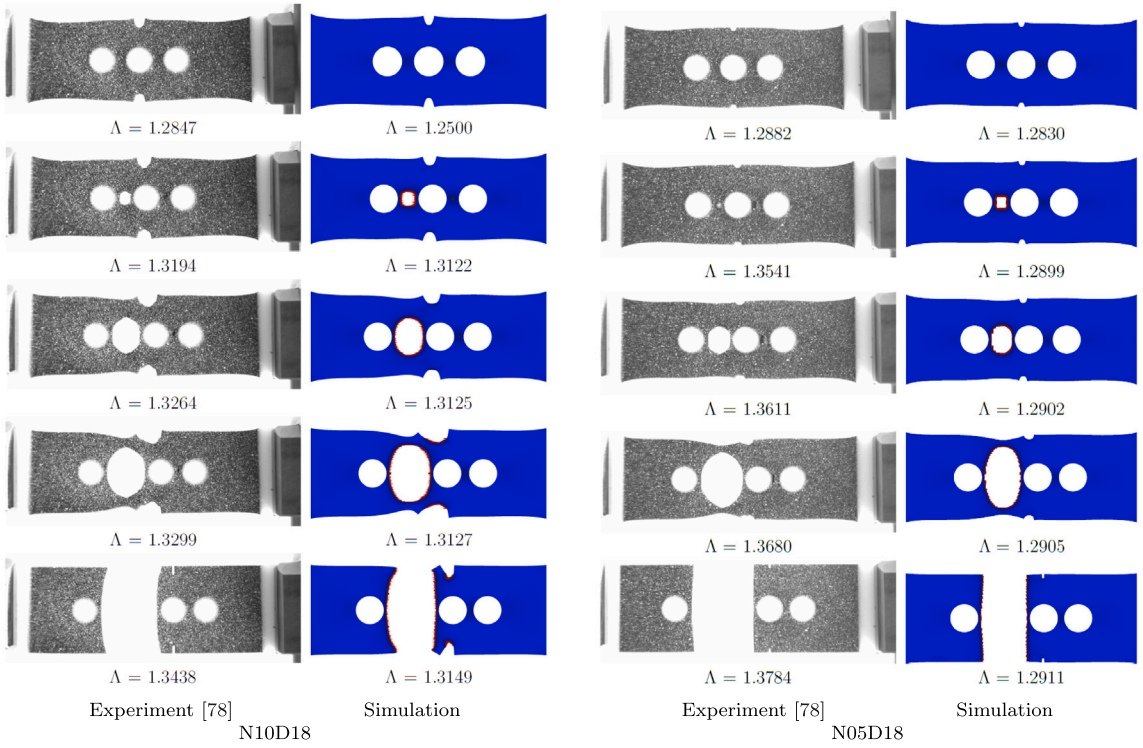

Fig. 19. Damage contour [ϕ] plots showing the crack initiation and propagation paths for different values of global stretch Λ compared to that of experiments conducted by Russ et al. [78]. Two specimen geometries namely N10D18 and N05D18 are compared here. To visualise the crack paths, all elements having $\phi > 0.85$ are removed here.

is also predicted by both Russ at al. [78] and Arunachala et al. [49].

Overall the phase field implementation yields very good prediction of the behaviour of all nine samples. The nature of deviations from the experimental results are in line with the implementations of both Russ at al. [78] and Arunachala at al. [49] pointing in the direction of uncertainties during manufacturing. It is important to note that a single set of calibrated parameters is used to model the behaviour of all nine samples thereby omitting any inconsistencies that may arise due to the complicated 3D printing process. Even though the implementation by Arunachala et al. [49] is an improvement over the 2D implementation by Russ et al. [78], the current implementation further improves the results leading to a better prediction.

5. Conclusions

A computational framework for predicting the rate-independent fracture behaviour of nearly incompressible hyperelastic material is presented here. The main novelty of the formulation lies in the use of the decoupled deviatoric and volumetric contributions to the strain energy density function which is appealing for modelling nearly incompressible materials. The perturbed Lagrangian scheme is used to realise the incompressibility of rubber-like materials and the resulting multi-field numerical framework is implemented in UEL of ABAQUS and solved using the BFGS monolithic solver. The novel framework alleviates the need for element deletion due to distorted elements even at large stretch values and multiple crack paths. The bulk energy contribution is degraded at a faster rate than the shear contribution to relax the incompressibility constraint in the fracture zone resulting in a smooth crack propagation. A thermodynamically consistent model is derived using two history variables arising from the shear and the volumetric energy parts. The prevention of damage healing is established using the history fields and is illustrated for a simple 1D problem involving cyclic loading. Further, the proposed scheme is tested for several examples where the predictions are compared to that of experiments. Firstly, tension test is performed on double edged notch specimen having five different pre-crack lengths. The load displacement results of the numerical predictions match well with that of the experimental results. Secondly, an out of plane tearing test is performed to illustrate the numerical robustness of the scheme even at large stretch values for the damaged elements. Lastly, a composite specimen made of soft matrix material having rigid inclusions is tested. A parametric study is performed whereby a total of nine specimens having different inclusion spacing and pre-crack lengths are considered. The results of the numerical prediction closely match the experimental results illustrating the ability of the scheme to predict the load displacement behaviour as well as complex crack paths. All the examples studied here yielded good results alleviating any difficulties arising from mesh distortion and incompressibility. For the first time, a true deviatoric–volumetric split-based constitutive model, coupled with the AT2 phase field model, has been implemented to simulate the fracture of nearly incompressible rubber-like materials. Future work will focus

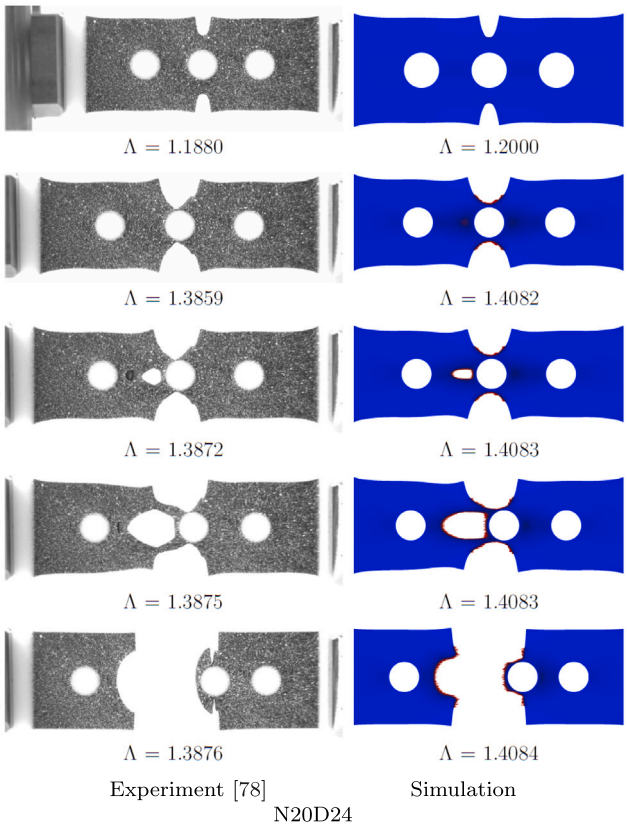

Fig. 20. Damage contour [ϕ] plots showing the crack initiation and propagation paths for different values of global stretch Λ compared to that of experiments conducted by Russ et al. [78]. To visualise the crack paths, all elements having $\phi > 0.85$ are removed here.

on extending this model to incorporate viscoelastic characteristics and cyclic fatigue damage models. The implementation of this numerical framework in the commercial software ABAQUS allows for its easy adaptation in the design optimisation of complex devices made from rubber-like polymers, reducing the need for costly experiments.

In the future, viscoelastic models can be incorporated to capture the effects of the rate dependent dissipation. A further extension to anisotropic modelling can overcome the limitation of the current model leading to the simulation of sideways cracking at large strain in the case of highly crosslinked elastomers. Finally, a fatigue damage model backed by experimental results will further enhance the numerical modelling capability for rubber-like materials.

CRediT authorship contribution statement

Deepak George: Writing – original draft, Visualization, Validation, Methodology, Investigation. **Shabnam Konica:** Writing – review & editing, Formal analysis. **Ian Masters:** Writing – review & editing, Supervision. **Mokarram Hossain:** Writing – review & editing, Writing – original draft, Funding acquisition, Conceptualization.

Declaration of competing interest

The authors declare that they have no known competing financial interests or personal relationships that could have appeared to influence the work reported in this paper.

Acknowledgment

This work was supported by the MEECE project funded by the European Regional Development Fund and the UK & Welsh governments through the Swansea Bay City Deal.

Data availability

No data was used for the research described in the article.

References

[1] J. Yang, Z. Liao, M. Hossain, G. Huang, K. Wang, X. Yao, Thermo-mechanical experimental investigations of 3D-printed elastomeric polyurethane from low to intermediate strain rates, Mech. Res. Commun. 134 (2023) 104212, http://dx.doi.org/10.1016/j.mechrescom.2023.104212.

[2] K.B. Putra, X. Tian, J. Plott, A. Shih, Biaxial test and hyperelastic material models of silicone elastomer fabricated by extrusion-based additive manufacturing for wearable biomedical devices, J. Mech. Behav. Biomed. Mater. 107 (2020) 103733, http://dx.doi.org/10.1016/j.jmbbm.2020.103733.

[3] H. Eggert, W. Kauschke, Structural Bearings, Wiley VCH, Germany, 2002.

[4] C. Porter, B. Zaman, R. Pazur, A critical examination of the shelf life of nitrile rubber O-Rings used in aerospace sealing applications, Polym. Degrad. Stab. 206 (2022) 110199, http://dx.doi.org/10.1016/j.polymdegradstab.2022.110199.

[5] A. Bera, D. Ganguly, S.K. Ghorai, J.P. Rath, S. Ramakrishnan, J. Kuriakose, S. Amarnath, S. Chattopadhyay, Treatment of natural rubber with bio-based components: A green endeavor to diminish the silica agglomeration for tyre tread application, Chem. Eng. J. Adv. 11 (2022) 100349, http://dx.doi.org/10.1016/j.ceja.2022.100349.

[6] N.H. Cohrs, A. Petrou, M. Loepfe, M. Yliruka, C.M. Schumacher, A.X. Kohll, C.T. Starck, M. Schmid Daners, M. Meboldt, V. Falk, W.J. Stark, A soft total artificial heart—First concept evaluation on a hybrid mock circulation, Artif. Organs. 41 (10) (2017) 948–958, http://dx.doi.org/10.1111/aor.12956.

[7] I. Collins, M. Hossain, W. Dettmer, I. Masters, Flexible membrane structures for wave energy harvesting: A review of the developments, materials and computational modelling approaches, Renew. Sustain. Energy Rev. 151 (2021) 111478, http://dx.doi.org/10.1016/j.rser.2021.111478.

[8] D. George, I. Collins, I. Masters, M. Hossain, Extreme load analysis of flexible wave energy converters utilising nonlocal continuum damage mechanics, Appl. Ocean Res. 142 (2024) 103843, http://dx.doi.org/10.1016/j.apor.2023.103843.

[9] A. Esmaeili, D. George, I. Masters, M. Hossain, Biaxial experimental characterizations of soft polymers: A review, Polym. Test. 128 (2023) 108246, http://dx.doi.org/10.1016/j.polymertesting.2023.108246.

[10] C. Miehe, S. Teichtmeister, F. Aldakheel, Phase-field modelling of ductile fracture: a variational gradient-extended plasticity-damage theory and its micromorphic regularization, Phil. Trans. R. Soc. A 374 (2066) (2016) 20150170, http://dx.doi.org/10.1098/rsta.2015.0170.

[11] W. Tan, E. Martínez-Pañeda, Phase field fracture predictions of microscopic bridging behaviour of composite materials, Compos. Struct. 286 (2022) 115242, http://dx.doi.org/10.1016/j.compstruct.2022.115242.

[12] W. Tan, E. Martínez-Pañeda, Phase field predictions of microscopic fracture and R-curve behaviour of fibre-reinforced composites, Compos. Sci. Technol. 202 (2021) 108539, http://dx.doi.org/10.1016/j.compscitech.2020.108539.

[13] E. de Souza Neto, D. Perić, M. Dutko, D. Owen, Design of simple low order finite elements for large strain analysis of nearly incompressible solids, Int. J. Solids Struct. 33 (20) (1996) 3277–3296, http://dx.doi.org/10.1016/0020-7683(95)00259-6.

[14] E.A.S. Neto, F.M.A. Pires, D.R.J. Owen, F-bar-based linear triangles and tetrahedra for finite strain analysis of nearly incompressible solids. Part I: formulation and benchmarking, Internat. J. Numer. Methods Engrg. 62 (3) (2005) 353–383, http://dx.doi.org/10.1002/nme.1187.

[15] D.P. Flanagan, T. Belytschko, A uniform strain hexahedron and quadrilateral with orthogonal hourglass control, Internat. J. Numer. Methods Engrg. 17 (5) (1981) 679–706, http://dx.doi.org/10.1002/nme.1620170504.

[16] T. Belytschko, J.S.-J. Ong, W.K. Liu, J.M. Kennedy, Hourglass control in linear and nonlinear problems, Comput. Methods Appl. Mech. Engrg. 43 (3) (1984) 251–276, http://dx.doi.org/10.1016/0045-7825(84)90067-7.

[17] P. Wriggers, J. Korelc, On enhanced strain methods for small and finite deformations of solids, Comput. Mech. 18 (6) (1996) 413–428, http://dx.doi.org/10.1007/BF00350250.

[18] J. Korelc, U. Šolinc, P. Wriggers, An improved EAS brick element for finite deformation, Comput. Mech. 46 (4) (2010) 641–659, http://dx.doi.org/10.1007/s00466-010-0506-0.

[19] J. Chen, W. Han, C. Wu, W. Duan, On the perturbed Lagrangian formulation for nearly incompressible and incompressible hyperelasticity, Comput. Methods Appl. Mech. Engrg. 142 (3) (1997) 335–351, http://dx.doi.org/10.1016/S0045-7825(96)01139-5.

[20] J. Simo, R. Taylor, K. Pister, Variational and projection methods for the volume constraint in finite deformation elasto-plasticity, Comput. Methods Appl. Mech. Engrg. 51 (1) (1985) 177–208, http://dx.doi.org/10.1016/0045-7825(85)90033-7.

[21] C. Kadapa, M. Hossain, A linearized consistent mixed displacement-pressure formulation for hyperelasticity, Mech. Adv. Mater. Struct. 29 (2) (2022) 267–284, http://dx.doi.org/10.1080/15376494.2020.1762952.

[22] C. Kadapa, Mixed displacement–pressure formulations and suitable finite elements for multimaterial problems with compressible and incompressible models, Comput. Methods Appl. Mech. Engrg. 432 (2024) 117354, http://dx.doi.org/10.1016/j.cma.2024.117354.

[23] C. Kadapa, Mixed Galerkin and Least-Squares Formulations for Isogeometric Analysis (Ph.D. thesis), Swansea University, Swansea, UK, 2014, Available at https://cronfa.swan.ac.uk/Record/cronfa42221.

[24] L.M. Kachanov, Time of the rupture process under creep conditions, Izvestija Akad. Nauk Sojuza Sovetskich Social. Resp. 8 (1958) 26–31.

[25] N. Moës, J. Dolbow, T. Belytschko, A finite element method for crack growth without remeshing, Internat. J. Numer. Methods Engrg. 46 (1) (1999) 131–150, http://dx.doi.org/10.1002/(SICI)1097-0207(19990910)46:1<131::AID-NME726>3.0.CO;2-J.

[26] T.Q. Bui, X. Hu, A review of phase-field models, fundamentals and their applications to composite laminates, Eng. Fract. Mech. 248 (2021) 107705, http://dx.doi.org/10.1016/j.engfracmech.2021.107705.

[27] Z.P. Bažant, M. Jirásek, Nonlocal integral formulations of plasticity and damage: Survey of progress, J. Eng. Mech. 128 (11) (2002) 1119–1149, http://dx.doi.org/10.1061/(ASCE)0733-9399(2002)128:11(1119).

[28] Z.P. Bažant, G. Pijaudier-Cabot, Nonlocal continuum damage, localization instability and convergence, J. Appl. Mech. 55 (2) (1988) 287–293, http://dx.doi.org/10.1115/1.3173674.

[29] R.H.J. Peerlings, R.D. Borst, W.A.M. Brekelmans, J.H.P.D. Vree, Gradient enhanced damage for quasi-brittle materials, Internat. J. Numer. Methods Engrg. 39 (19) (1996) 3391–3403, http://dx.doi.org/10.1002/(SICI)1097-0207(19961015)39:19<3391::AID-NME7>3.0.CO;2-D.

[30] P. Steinmann, Formulation and computation of geometrically non-linear gradient damage, Internat. J. Numer. Methods Engrg. 46 (5) (1999) 757–779, http://dx.doi.org/10.1002/(SICI)1097-0207(19991020)46:5<757::AID-NME731>3.0.CO;2-N.

[31] T. Waffenschmidt, C. Polindara, A. Menzel, S. Blanco, A gradient-enhanced large-deformation continuum damage model for fibre-reinforced materials, Comput. Methods Appl. Mech. Engrg. 268 (2014) 801–842, http://dx.doi.org/10.1016/j.cma.2013.10.013.

[32] S. Silling, Reformulation of elasticity theory for discontinuities and long-range forces, J. Mech. Phys. Solids 48 (1) (2000) 175–209, http://dx.doi.org/10.1016/S0022-5096(99)00029-0.

[33] E. Madenci, Peridynamic integrals for strain invariants of homogeneous deformation, ZAMM - J. Appl. Math. Mech. / Z. Angew. Math. Mech. 97 (10) (2017) 1236–1251, http://dx.doi.org/10.1002/zamm.201600242.

[34] D. Sulsky, Z. Chen, H. Schreyer, A particle method for history-dependent materials, Comput. Methods Appl. Mech. Engrg. 118 (1) (1994) 179–196, http://dx.doi.org/10.1016/0045-7825(94)90112-0.

[35] Y. Liang, X. Zhang, Y. Liu, Extended material point method for the three-dimensional crack problems, Internat. J. Numer. Methods Engrg. 122 (12) (2021) 3044–3069, http://dx.doi.org/10.1002/nme.6653.

[36] Z. Zhang, Z. Hu, H. Ye, H. Zhang, Y. Zheng, A mixed three-field total Lagrangian material point method for phase-field fracture modeling of nearly incompressible rubber-like solids, Internat. J. Numer. Methods Engrg. 124 (18) (2023) 4097–4117, http://dx.doi.org/10.1002/nme.7303.

[37] P. Steinmann, On spatial and material settings of hyperelastostatic crystal defects, J. Mech. Phys. Solids 50 (8) (2002) 1743–1766, http://dx.doi.org/10.1016/S0022-5096(01)00135-1.

[38] A. Menzel, R. Denzer, P. Steinmann, On the comparison of two approaches to compute material forces for inelastic materials. Application to single-slip crystal-plasticity, Comput. Methods Appl. Mech. Engrg. 193 (48) (2004) 5411–5428, http://dx.doi.org/10.1016/j.cma.2003.12.070.

[39] P. Steinmann, Spatial and Material Forces in Nonlinear Continuum Mechanics, Springer Cham, 2022, URL https://link.springer.com/book/10.1007/978-3-030-89070-4.

[40] M.A. Moreno-Mateos, P. Steinmann, Configurational force method enables fracture assessment in soft materials, J. Mech. Phys. Solids 186 (2024) 105602, http://dx.doi.org/10.1016/j.jmps.2024.105602.

[41] M.A. Moreno-Mateos, M. Mehnert, P. Steinmann, Electro-mechanical actuation modulates fracture performance of soft dielectric elastomers, Internat. J. Engrg. Sci. 195 (2024) 104008, http://dx.doi.org/10.1016/j.ijengsci.2023.104008.

[42] C. Miehe, L.-M. Schänzel, Phase field modeling of fracture in rubbery polymers. Part I: Finite elasticity coupled with brittle failure, J. Mech. Phys. Solids 65 (2014) 93–113, http://dx.doi.org/10.1016/j.jmps.2013.06.007.

[43] C. Hesch, K. Weinberg, Thermodynamically consistent algorithms for a finite-deformation phase-field approach to fracture, Internat. J. Numer. Methods Engrg. 99 (12) (2014) 906–924, http://dx.doi.org/10.1002/nme.4709.

[44] M.J. Borden, T.J. Hughes, C.M. Landis, A. Anvari, I.J. Lee, A phase-field formulation for fracture in ductile materials: Finite deformation balance law derivation, plastic degradation, and stress triaxiality effects, Comput. Methods Appl. Mech. Engrg. 312 (2016) 130–166, http://dx.doi.org/10.1016/j.cma.2016.09.005.

[45] S. Tang, G. Zhang, T.F. Guo, X. Guo, W.K. Liu, Phase field modeling of fracture in nonlinearly elastic solids via energy decomposition, Comput. Methods Appl. Mech. Engrg. 347 (2019) 477–494, http://dx.doi.org/10.1016/j.cma.2018.12.035.

[46] P.J. Loew, B. Peters, L.A. Beex, Rate-dependent phase-field damage modeling of rubber and its experimental parameter identification, J. Mech. Phys. Solids 127 (2019) 266–294, http://dx.doi.org/10.1016/j.jmps.2019.03.022.

[47] B. Yin, M. Kaliske, Fracture simulation of viscoelastic polymers by the phase-field method, Comput. Mech. 65 (2020) 293–309, http://dx.doi.org/10.1007/s00466-019-01769-1.

[48] F. Peng, W. Huang, Y. Ma, Z.-Q. Zhang, N. Fu, Fourth-order phase field model with spectral decomposition for simulating fracture in hyperelastic material, Fatigue Fract. Eng. Mater. Struct. 44 (9) (2021) 2372–2388, http://dx.doi.org/10.1111/ffe.13495.

[49] P.K. Arunachala, S. Abrari Vajari, M. Neuner, C. Linder, A multiscale phase field fracture approach based on the non-affine microsphere model for rubber-like materials, Comput. Methods Appl. Mech. Engrg. 410 (2023) 115982, http://dx.doi.org/10.1016/j.cma.2023.115982.

[50] P.K. Arunachala, S. Abrari Vajari, M. Neuner, J.S. Sim, R. Zhao, C. Linder, A multiscale anisotropic polymer network model coupled with phase field fracture, Internat. J. Numer. Methods Engrg. 125 (13) (2024) e7488, http://dx.doi.org/10.1002/nme.7488.

[51] A. Najmeddine, M. Shakiba, Physics and chemistry-based phase-field constitutive framework for thermo-chemically aged elastomer, Int. J. Mech. Sci. 262 (2024) 108721, http://dx.doi.org/10.1016/j.ijmecsci.2023.108721.

[52] D. Pranavi, P. Steinmann, A. Rajagopal, A unifying finite strain modeling framework for anisotropic mixed-mode fracture in soft materials, Comput. Mech. 73 (2024) 123–137, http://dx.doi.org/10.1007/s00466-023-02359-y.

[53] A. Valverde-González, J. Reinoso, N.K. Jha, J. Merodio, M. Paggi, A phase field approach to fracture for hyperelastic and visco-hyperelastic materials applied to pre-stressed cylindrical structures, Mech. Adv. Mater. Struct. 31 (4) (2024) 749–768, http://dx.doi.org/10.1080/15376494.2022.2121452.

[54] F. Dammaß, K.A. Kalina, M. Ambati, M. Kästner, Phase-field modelling and analysis of rate-dependent fracture phenomena at finite deformation, Comput. Mech. 72 (2023) 859–883, http://dx.doi.org/10.1007/s00466-023-02310-1.

[55] S. Swamynathan, S. Jobst, M.-A. Keip, An energetically consistent tension–compression split for phase-field models of fracture at large deformations, Mech. Mater. 157 (2021) 103802, http://dx.doi.org/10.1016/j.mechmat.2021.103802.

[56] F. Peng, W. Huang, Z.-Q. Zhang, T. Fu Guo, Y. Ma, Phase field simulation for fracture behavior of hyperelastic material at large deformation based on edge-based smoothed finite element method, Eng. Fract. Mech. 238 (2020) 107233, http://dx.doi.org/10.1016/j.engfracmech.2020.107233.

[57] J. Reinoso, A. Arteiro, M. Paggi, P. Camanho, Strength prediction of notched thin ply laminates using finite fracture mechanics and the phase field approach, Compos. Sci. Technol. 150 (2017) 205–216, http://dx.doi.org/10.1016/j.compscitech.2017.07.020.

[58] F.A. Denli, O. Gültekin, A.G. Holzapfel, H. Dal, A phase-field model for fracture of unidirectional fiber-reinforced polymer matrix composites, Comput. Mech. 65 (2020) 1149–1166, http://dx.doi.org/10.1007/s00466-019-01812-1.

[59] T.K. Mandal, V.P. Nguyen, J.-Y. Wu, A length scale insensitive anisotropic phase field fracture model for hyperelastic composites, Int. J. Mech. Sci. 188 (2020) 105941, http://dx.doi.org/10.1016/j.ijmecsci.2020.105941.

[60] S. Konica, T. Sain, Phase-field fracture modeling for unidirectional fiber-reinforced polymer composites, Eur. J. Mech. A Solids 100 (2023) 105035, http://dx.doi.org/10.1016/j.euromechsol.2023.105035.

[61] S. Konica, Oxidative Aging and Fracture Behavior of Polymers and Composites: Theory, Modeling and Experiments (Ph.D. thesis), 2022, p. 308, URL https://www.proquest.com/dissertations-theses/oxidative-aging-fracture-behavior-polymers/docview/2665111562/se-2.

[62] P. Kumar, P. Steinmann, J. Mergheim, A graded interphase enhanced phase-field approach for modeling fracture in polymer composites, Forces Mech. 9 (2022) 100135, http://dx.doi.org/10.1016/j.finmec.2022.100135.

[63] M. Marulli, A. Valverde-González, A. Quintanas-Corominas, M. Paggi, J. Reinoso, A combined phase-field and cohesive zone model approach for crack propagation in layered structures made of nonlinear rubber-like materials, Comput. Methods Appl. Mech. Engrg. 395 (2022) 115007, http://dx.doi.org/10.1016/j.cma.2022.115007.

[64] A. Raina, C. Miehe, A phase-field model for fracture in biological tissues, Biomech. Model. Mechanobiol. 15 (2016) 479–496, http://dx.doi.org/10.1007/s10237-015-0702-0.

[65] O. Gültekin, H. Dal, G.A. Holzapfel, A phase-field approach to model fracture of arterial walls: Theory and finite element analysis, Comput. Methods Appl. Mech. Engrg. 312 (2016) 542–566, http://dx.doi.org/10.1016/j.cma.2016.04.007.

[66] F. Tian, J. Zeng, X. Tang, T. Xu, L. Li, A dynamic phase field model with no attenuation of wave speed for rapid fracture instability in hyperelastic materials, Int. J. Solids Struct. 202 (2020) 685–698, http://dx.doi.org/10.1016/j.ijsolstr.2020.07.004.

[67] S. Zheng, H. You, H. Li, K. Lam, A model for fracture of temperature-sensitive hydrogel with diffusion and large deformation, Eng. Fract. Mech. 281 (2023) 109138, http://dx.doi.org/10.1016/j.engfracmech.2023.109138.

[68] J. Ji, M. Zhang, J. Zeng, F. Tian, Uncovering the intrinsic deficiencies of phase-field modeling for dynamic fracture, Int. J. Solids Struct. 256 (2022) 111961, http://dx.doi.org/10.1016/j.ijsolstr.2022.111961.

[69] Y. Mao, L. Anand, A theory for fracture of polymeric gels, J. Mech. Phys. Solids 115 (2018) 30–53, http://dx.doi.org/10.1016/j.jmps.2018.02.008.

[70] G. Zhang, T.F. Guo, Z. Zhou, S. Tang, X. Guo, A phase-field model for fracture in water-containing soft solids, Eng. Fract. Mech. 212 (2019) 180–196, http://dx.doi.org/10.1016/j.engfracmech.2019.02.035.

[71] S. Zheng, R. Huang, R. Lin, Z. Liu, A phase field solution for modelling hyperelastic material and hydrogel fracture in ABAQUS, Eng. Fract. Mech. 276 (2022) 108894, http://dx.doi.org/10.1016/j.engfracmech.2022.108894.

[72] G. Zhang, C. Tang, P. Chen, G. Long, J. Cao, S. Tang, Advancements in phase-field modeling for fracture in nonlinear elastic solids under finite deformations, Mathematics 11 (15) (2023) http://dx.doi.org/10.3390/math11153366.

[73] M.A. Moreno-Mateos, M. Hossain, P. Steinmann, D. Garcia-Gonzalez, Hard magnetics in ultra-soft magnetorheological elastomers enhance fracture toughness and delay crack propagation, J. Mech. Phys. Solids 173 (2023) 105232, http://dx.doi.org/10.1016/j.jmps.2023.105232.
[74] C. Miehe, F. Aldakheel, A. Raina, Phase field modeling of ductile fracture at finite strains: A variational gradient-extended plasticity-damage theory, Int. J. Plast. 84 (2016) 1–32, http://dx.doi.org/10.1016/j.ijplas.2016.04.011.
[75] C. Miehe, H. Dal, L.-M. Schänzel, A. Raina, A phase-field model for chemo-mechanical induced fracture in lithium-ion battery electrode particles, Internat. J. Numer. Methods Engrg. 106 (9) (2016) 683–711, http://dx.doi.org/10.1002/nme.5133.
[76] X. Cao, Y. Lu, Z. Chen, K. Zhang, F. Wang, A chemo-mechanical phase-field framework for dynamic fracture with viscoplastic flow for large-deformed electrode in lithium-ion batteries, J. Alloys Compd. 965 (2023) 171387, http://dx.doi.org/10.1016/j.jallcom.2023.171387.
[77] S. Konica, B.W. Sheldon, V. Srivastava, Role of coupled electrochemistry and stress on the Li-anode instability: A continuum approach, 2024, http://dx.doi.org/10.48550/arXiv.2405.05837.
[78] J. Russ, V. Slesarenko, S. Rudykh, H. Waisman, Rupture of 3D-printed hyperelastic composites: Experiments and phase field fracture modeling, J. Mech. Phys. Solids 140 (2020) 103941, http://dx.doi.org/10.1016/j.jmps.2020.103941.
[79] P. Aurojyoti, A. Rajagopal, K. Reddy, Modeling fracture in polymeric material using phase field method based on critical stretch criterion, Int. J. Solids Struct. 270 (2023) 112216, http://dx.doi.org/10.1016/j.ijsolstr.2023.112216.
[80] C. Xing, T. Yu, Y. Sun, Y. Wang, An adaptive phase-field model with variable-node elements for fracture of hyperelastic materials at large deformations, Eng. Fract. Mech. 281 (2023) 109115, http://dx.doi.org/10.1016/j.engfracmech.2023.109115.
[81] J. Lee, S. Lee, S.A. Chester, H. Cho, Finite element implementation of a gradient-damage theory for fracture in elastomeric materials, Int. J. Solids Struct. 279 (2023) 112309, http://dx.doi.org/10.1016/j.ijsolstr.2023.112309.
[82] J. Ciambella, G. Lancioni, N. Stortini, An Ogden-like formulation incorporating phase-field fracture in elastomers: from brittle to pseudo-ductile failures, Phil. Trans. R. Soc. A 380 (2234) (2022) 20210323, http://dx.doi.org/10.1098/rsta.2021.0323.
[83] R. Brighenti, T. Rabczuk, X. Zhuang, Phase field approach for simulating failure of viscoelastic elastomers, Eur. J. Mech. A Solids 85 (2021) 104092, http://dx.doi.org/10.1016/j.euromechsol.2020.104092.
[84] Z. Ma, X. Feng, W. Hong, Fracture of soft elastic foam, J. Appl. Mech. 83 (3) (2015) 031007, http://dx.doi.org/10.1115/1.4032050.
[85] B. Li, N. Bouklas, A variational phase-field model for brittle fracture in polydisperse elastomer networks, Int. J. Solids Struct. 182–183 (2020) 193–204, http://dx.doi.org/10.1016/j.ijsolstr.2019.08.012.
[86] J.-Y. Ye, L.-W. Zhang, J. Reddy, Large strained fracture of nearly incompressible hyperelastic materials: Enhanced assumed strain methods and energy decomposition, J. Mech. Phys. Solids 139 (2020) 103939, http://dx.doi.org/10.1016/j.jmps.2020.103939.
[87] F. Tian, J. Zeng, M. Zhang, L. Li, Mixed displacement–pressure-phase field framework for finite strain fracture of nearly incompressible hyperelastic materials, Comput. Methods Appl. Mech. Engrg. 394 (2022) 114933, http://dx.doi.org/10.1016/j.cma.2022.114933.
[88] I. Ang, N. Bouklas, B. Li, Stabilized formulation for phase-field fracture in nearly incompressible hyperelasticity, Internat. J. Numer. Methods Engrg. 123 (19) (2022) 4655–4673, http://dx.doi.org/10.1002/nme.7050.
[89] A.A. Griffith, G.I. Taylor, The phenomena of rupture and flow in solids, Philos. Trans. R. Soc. Lond. Ser. A Contain. Pap. Math. Phys. Character 221 (582–593) (1921) 163–198, http://dx.doi.org/10.1098/rsta.1921.0006.
[90] G. Francfort, J.-J. Marigo, Revisiting brittle fracture as an energy minimization problem, J. Mech. Phys. Solids 46 (8) (1998) 1319–1342, http://dx.doi.org/10.1016/S0022-5096(98)00034-9.
[91] L. Ambrosio, V.M. Tortorelli, Approximation of functional depending on jumps by elliptic functional via Γ -convergence, Comm. Pure Appl. Math. 43 (8) (1990) 999–1036, http://dx.doi.org/10.1002/cpa.3160430805.
[92] B. Bourdin, G. Francfort, J.-J. Marigo, Numerical experiments in revisited brittle fracture, J. Mech. Phys. Solids 48 (4) (2000) 797–826, http://dx.doi.org/10.1016/S0022-5096(99)00028-9.
[93] K. Pham, H. Amor, J.J. Marigo, C. Maurini, Gradient damage models and their use to approximate brittle fracture, Int. J. Damage Mech. 20 (4) (2011) 618–652, http://dx.doi.org/10.1177/1056789510386852.
[94] M. Ambati, T. Gerasimov, L. De Lorenzis, A review on phase-field models of brittle fracture and a new fast hybrid formulation, Comput. Mech. 55 (2) (2015) 383–405, http://dx.doi.org/10.1007/s00466-014-1109-y.
[95] S. Sun, Q. Gong, Y. Ni, M. Yi, A micromagnetic-mechanically coupled phase-field model for fracture and fatigue of magnetostrictive alloys, J. Mech. Phys. Solids 191 (2024) 105767, http://dx.doi.org/10.1016/j.jmps.2024.105767.
[96] A. Braides, A. Garroni, On the non-local approximation of free-discontinuity problems, Comm. Partial Differential Equations 23 (5–6) (1998) 817–829, http://dx.doi.org/10.1080/03605309808821367.
[97] P. Carrara, M. Ambati, R. Alessi, L. De Lorenzis, A framework to model the fatigue behavior of brittle materials based on a variational phase-field approach, Comput. Methods Appl. Mech. Engrg. 361 (2020) 112731, http://dx.doi.org/10.1016/j.cma.2019.112731.
[98] L. Ambrosio, On the approximation of free discontinuity problems, Boll. Unione Mat. Ital. B (7) (1992) 105–123.
[99] C. Miehe, J. Keck, Superimposed finite elastic–viscoelastic–plastoelastic stress response with damage in filled rubbery polymers. Experiments, modelling and algorithmic implementation, J. Mech. Phys. Solids 48 (2) (2000) 323–365, http://dx.doi.org/10.1016/S0022-5096(99)00017-4.
[100] P.K. Kristensen, C.F. Niordson, E. Martínez-Pañeda, An assessment of phase field fracture: crack initiation and growth, Phil. Trans. R. Soc. A 379 (2203) (2021) 20210021, http://dx.doi.org/10.1098/rsta.2021.0021.
[101] P. Steinmann, M. Hossain, G. Possart, Hyperelastic models for rubber-like materials: consistent tangent operators and suitability for Treloar's data, Arch. Appl. Mech. 82 (9) (2012) 1183–1217, http://dx.doi.org/10.1007/s00419-012-0610-z.
[102] M. Hossain, P. Steinmann, More hyperelastic models for rubber-like materials: consistent tangent operators and comparative study, J. Mech. Behav. Mater. 22 (1–2) (2013) http://dx.doi.org/10.1515/jmbm-2012-0007.
[103] G. Marckmann, E. Verron, Comparison of hyperelastic models for rubber-like materials, Rubber Chem. Technol. 79 (5) (2006) 835–858, http://dx.doi.org/10.5254/1.3547969.
[104] M. Hossain, A. Amin, M.N. Kabir, Eight-chain and full-network models and their modified versions for rubber hyperelasticity: a comparative study, J. Mech. Behav. Mater. 24 (1–2) (2015) 11–24, http://dx.doi.org/10.1515/jmbm-2015-0002.
[105] G.A. Holzapfel, Nonlinear Solid Mechanics: A Continuum Approach for Engineering, John Wiley & Sons, UK, 2000, URL https://www.ebook.de/de/product/3056011/holzapfel_nonlinear_solid_mechanics.html.
[106] Z. Li, J. Wang, M. Hossain, C. Kadapa, A general theoretical scheme for shape-programming of incompressible hyperelastic shells through differential growth, Int. J. Solids Struct. 265–266 (2023) 112128, http://dx.doi.org/10.1016/j.ijsolstr.2023.112128.
[107] C. Kadapa, M. Hossain, A unified numerical approach for soft to hard magneto-viscoelastically coupled polymers, Mech. Mater. 166 (2022) 104207, http://dx.doi.org/10.1016/j.mechmat.2021.104207.
[108] C. Kadapa, Z. Li, M. Hossain, J. Wang, On the advantages of mixed formulation and higher-order elements for computational morphoelasticity, J. Mech. Phys. Solids 148 (2021) 104289, http://dx.doi.org/10.1016/j.jmps.2020.104289.
[109] C. Kadapa, A novel semi-implicit scheme for elastodynamics and wave propagation in nearly and truly incompressible solids, Acta Mech. 232 (6) (2021) 2135–2163, http://dx.doi.org/10.1007/s00707-020-02883-5.
[110] C. Kadapa, M. Hossain, A robust and computationally efficient finite element framework for coupled electromechanics, Comput. Methods Appl. Mech. Engrg. 372 (2020) 113443, http://dx.doi.org/10.1016/j.cma.2020.113443.

[111] B. Bourdin, G.A. Francfort, J.-J. Marigo, The variational approach to fracture, J. Elasticity 91 (2008) 5–148, http://dx.doi.org/10.1007/s10659-007-9107-3.
[112] S. May, J. Vignollet, R. de Borst, A new arc-length control method based on the rates of the internal and the dissipated energy, Eng. Comput. 33 (2016) 100–115, http://dx.doi.org/10.1108/EC-02-2015-0044.
[113] T. Gerasimov, L. De Lorenzis, A line search assisted monolithic approach for phase-field computing of brittle fracture, Comput. Methods Appl. Mech. Engrg. 312 (2016) 276–303, http://dx.doi.org/10.1016/j.cma.2015.12.017.
[114] T. Heister, M.F. Wheeler, T. Wick, A primal-dual active set method and predictor-corrector mesh adaptivity for computing fracture propagation using a phase-field approach, Comput. Methods Appl. Mech. Engrg. 290 (2015) 466–495, http://dx.doi.org/10.1016/j.cma.2015.03.009.
[115] T. Wick, Modified Newton methods for solving fully monolithic phase-field quasi-static brittle fracture propagation, Comput. Methods Appl. Mech. Engrg. 325 (2017) 577–611, http://dx.doi.org/10.1016/j.cma.2017.07.026.
[116] J.-Y. Wu, Y. Huang, V.P. Nguyen, On the BFGS monolithic algorithm for the unified phase field damage theory, Comput. Methods Appl. Mech. Engrg. 360 (2020) 112704, http://dx.doi.org/10.1016/j.cma.2019.112704.
[117] P.K. Kristensen, E. Martínez-Pañeda, Phase field fracture modelling using quasi-Newton methods and a new adaptive step scheme, Theor. Appl. Fract. Mech. 107 (2020) 102446, http://dx.doi.org/10.1016/j.tafmec.2019.102446.
[118] H. Matthies, G. Strang, The solution of nonlinear finite element equations, Internat. J. Numer. Methods Engrg. 14 (11) (1979) 1613–1626, http://dx.doi.org/10.1002/nme.1620141104.
[119] N.A. Hocine, M.N. Abdelaziz, A. Imad, Fracture problems of rubbers: J-integral estimation based upon η factors and an investigation on the strain energy density distribution as a local criterion, Int. J. Fract. 117 (2002) 1–23, http://dx.doi.org/10.1023/A:1020967429222.
[120] C. Miehe, L.-M. Schänzel, H. Ulmer, Phase field modeling of fracture in multi-physics problems. Part I. Balance of crack surface and failure criteria for brittle crack propagation in thermo-elastic solids, Comput. Methods Appl. Mech. Engrg. 294 (2015) 449–485, http://dx.doi.org/10.1016/j.cma.2014.11.016.